IEEE Access
Multidisciplinary | Rapid Review | Open Access Journal

Received 13 December 2023, accepted 19 January 2024, date of publication 25 January 2024, date of current version 1 February 2024.

Digital Object Identifier 10.1109/ACCESS.2024.3358425

RESEARCH ARTICLE

Frequency Regulation in Interconnected Power System Through Enhanced Beluga Whale Optimized Flatness-Based Active Disturbance Rejection Control

SHAHZAD ALI[1], YUANQING XIA[1], (Fellow, IEEE), ZOHAIB AHMAD KHAN[1], ABID ALI[1], QAMAR NAVID[1], KHURSHEED AURANGZEB[2], (Senior Member, IEEE), AND MUHAMMAD SHAHID ANWAR[3]

[1]School of Automation, Beijing Institute of Technology, Beijing 100081, China
[2]Department of Computer Engineering, College of Computer and Information Sciences, King Saud University, Riyadh 11543, Saudi Arabia
[3]Department of AI and Software, Gachon University, Seongnam-si 13120, South Korea

Corresponding author: Yuanqing Xia (xia_yuanqing@bit.edu.cn)

This Research is funded by Researchers Supporting Project Number (RSPD2024R947), King Saud University, Riyadh, Saudi Arabia.

ABSTRACT Ever-increasing dynamic surges in renewable-based electric power systems, notably wind and photovoltaic farms bring adverse impacts and challenges in terms of reliability and stability. The intermittency of renewable sources imposes significant deviations in frequency due to variations in demand. Wind power induces instability in the grid due to its vulnerable nature, and reduction in system inertia. To mitigate these dynamics issues, an optimal control technique based on flatness-based Active disturbance rejection control (FADRC) and utilizing an enhanced Beluga Whale optimization algorithm (EBWO) for a multi-area interconnected power system with photovoltaic generation. The proposed LFC model addresses the load perturbation and the deviation of tie-line power, with system uncertainties considered as lumped disturbances that are approximated by extended state observers. To achieve optimal performance, the Enhanced Beluga Whale optimization algorithm is adopted and integrated with the suggested controller to fine-tune the controller. To validate the formidable performance of the suggested scheme, different cases have been studied with the existing approaches. The simulation results reveal the supremacy and robustness of the dynamic response of the Flatness-based active disturbance rejection control as compared to other approaches under load variations and parameter uncertainty.

INDEX TERMS Flatness-based Active disturbance rejection control, beluga whale optimization algorithm, Photovoltaic generation, multi-area interconnected power systems, renewable sources.

NOMENCLATURE

Abbreviations

AGC	Automatic generation control.
BWO	Beluga Whale optimization algorithm.
BWO	Beluga Whale optimization.
BWs	Beluga Whales.
EBWO	Enhanced Beluga Whale optimization algorithm.
ESO	Extended state observer.
FADRC	Flatness based active disturbance rejection control.
HHO	Haris hawk optimizer.
IMC	Internal mode control.
ITAE	Integral time absolute error.
LADRC	Linear active disturbance rejection control.
LFC	Load frequency control.
MPPT	Maximum power point tracking.
PID	Proportional integral derivative.
PSs	Power system.

The associate editor coordinating the review of this manuscript and approving it for publication was Wonhee Kim.

PV	Photovoltaic system.
RESs	Renewable energy sources.
SMC	Sliding mode control.
WT	Wind turbine.

System dynamics

α_1, α_2	Negative zero, Pv system gain,.
α_3, α_4	Negative poles.
ΔACE	Area control error.
Δf_i	Frequency deviation.
ΔK_r	Reheater gain.
$\Delta P_P V$	Solar power deviation.
ΔP_W	Wind Power Deviation.
ΔP_{Di}	Load Perturbation.
ΔP_{th}	Thermal Power Deviation.
ΔP_{tie}	Tie-line power deviation.
B, R	Frequency bias, droop gain.
H, D	Inertia constant, Droop coefficient.
K_{fc}, K_{pc}	Fluid coupling gain, Blade characteristics.
K_{P1}	Wind pitch control.
K_{P2}, K_{P3}	Gain of pitch actuator, data pitch.
T_W	Wind generation constant.
T_g, T_t, T_r	Time constant of governor, turbine, reheater.
T_{P1}, T_{P2}	Time constant of wind Pitch control, Pitch actuator.
T_{P3}	Data pitch time constant.

Optimization parameters

χ_i^T	Position of i_{th} beluga Whale.
χ_r^T	Represents a random selected beluga Whale.
χ_{step}	Step size of whale fall.
ω_c	Controller bandwidth.
ω_o	Observer bandwidth.
B_f	Equilibrium factor.
l_b, u_b	Lower and upper bounds.
L_f	Leavy flight.
r_i	Random number.
W_f	Represents the whale fall phase.

I. INTRODUCTION

The ever-increasing demand for electric power and the rapid increase of renewable energy sources (RESs) as a means of reducing the impact of climate change have captured significant attention in recent years [1]. Renewable energy sources (RESs) are environmentally friendly and cost-effective alternatives to fossil fuels. However, the stability and reliability of power systems can be compromised by the variability of RESs, such as solar and wind energy [2]. The utilization of RESs presents significant potential; yet, it introduces a degree of uncertainty in power supply due to factors such as weather conditions and daylight availability. Thus, variations in the active power demand and the intermittent characteristic of RESs may result in deviation in frequency and tie-line power. These variations may significantly affect the power system's overall functionality and stability [3]. However, severe frequency changes not only pose a significant risk to the power system equipment but also have the potential to trigger severe system failures [4]. Therefore, maintaining the balance between load demands and generation requires an efficient and reliable control mechanism.This control method, also known as Automatic Generation Control (AGC) or Load Frequency Control (LFC), is essential to the functioning of contemporary power systems.

In the last few decades, a considerable amount of research has been done on LFC schemes for frequency deviation and disturbance mitigation in single and multi-area power systems (PSs). Most widely traditional PID, PI controllers have been used in power systems for handling external disturbances. However, these control techniques are easy to implement but not robust against parameter uncertainties, resulting in maximum settling time and frequency deviation [5]. A PI controller is designed to deal with oscillations and stability issues due to communication delays, but the approach is straightforward [6]. One of the challenges of PI-LFC is to find the optimal values of the PI parameters that can enhance the system performance. Various optimization methods have been proposed to solve this problem and adjust the PI parameters accordingly. A firefly algorithm-based PI [7], Harris Hawks optimizer (HHO) [8] has been explored. Besides, robust control techniques have been utilized for the LFC problem, a PSO-based sliding mode controller (SMC) [9], an ESO based Second-order SMC [10], a PSO tuned Linear active disturbance rejection control (LADRC) for multi-area power systems with high wind penetration [11], dual loop internal mode control (IMC) [12]. A type-2 fuzzy fractional order PID based on a multi-objective optimization algorithm for the LFC issue in an interconnected PSs has been introduced without considering the RESs [13].

Additionally, to overcome the ever-increasing energy demand and mitigate environmental emissions, RESs have been integrated into the power system [14]. Among RESs, the wind power system is the most advanced and widely employed in power generation [15]. With the perpetual penetration of renewable sources and their intermittent nature, LFC has become a challenging problem to deal with increasing unpredictability and inconsistency in generation [16], [17]. PI-TID [3] and PID [18] controllers based on chaotic butterfly optimization and black widow optimization algorithms have been introduced to improve the LFC capabilities of the interconnected PSs including RESs. Multi-objective optimization algorithm based fractional order PID without considering the RESs [19] and fractional order brain emotion learning based intelligent controller is employed to actively reduces the deviation of frequency and tie-line power [20]. Quasi-oppositional harmony search optimization based fractional order fuzzy PID has been utilized in a power system including a wind turbine [21]. Considering the impact of wind and solar-thermal, a fuzzy

PD-PI cascade controller [22], based on the grasshopper optimization algorithm. a PD with filter cascade PI LFC technique has been utilized to gain a robust performance in the presence of uncertainties and load perturbations [23].

In the preceding literature, the LFC methods are established based on a thorough knowledge of the system, where the system reliability is a prime priority. However, uncertainties in the dynamics of real-time power systems, errors in modeling and unmodeled dynamics, parameter perturbation, and instantaneous load changes. Hence, the LFC scheme for multi-area PSs should have an inherent property of robustness and adaptiveness against load perturbation and parameter variations which can adversely affect the system stability and reliability. Therefore, a well-equipped LFC scheme should be designed to estimate all of the uncertainties at once and compensate for them to maintain the system's performance. Therefore, to handle the external disturbance along with the un-modeled dynamics in a system, the ADRC approach has been proposed by Han [24]. The characteristic feature of the ADRC is to use the extended state observer, defines the extended states as lumped disturbances in addition to approximating the system states. Thus, the internal disturbances and parameter uncertainties caused by the un-modeled dynamics are lumped together as an extended state, which a PD control law can be used to compensate and estimate utilizing ESO [25]. The ESO operates independently of the mathematical model of disturbances, demanding only a modest detail of the controlled process for its implementation [26]. Although many parameters must be tuned, a linear ADRC [27] has been proposed to optimize only one parameter and facilitate its practical applications [28]. For a multi-area PS that includes non-linearities, a linear ADRC has been applied without taking RESs into account [29]. LADRC, based on Reinforcement learning, has been introduced to deal with extensive external disturbances [30] considering the non-linearities in the multi-power system. An effort has been made to integrate a DFIG-based wind turbine into the power system using a Linear-ADRC based on the modified bat to deal with the intermittent nature of wind and external disturbances with uncertainties in system parameters [31]. Furthermore, an extended form of the ADRC has been introduced based on the concept of differential flatness [32] and ADRC known as Flatness based ADRC(FADRC). The FADRC method uses the flatness property [33] to design an observer that estimates the system's state and disturbances and then uses the ADRC algorithm to compensate for the disturbances [34]. The flatness-based discrete ADRC has been applied to overcome the issue of non-minimum phase (NMP) zero in flexible transmission system [35]. Without taking RESs into account, an approximated flatness-based ADRC has been presented for the LFC of interconnected PSs [36].

Motivated by the growing complexity in power systems due to the integration of RESs because of their intermittent nature as analyzed from the above discussion, this research article proposes an application of flatness-based ADRC. Although numerous research works have investigated different variations of ADRC in power system control, a notable void remains in addressing the complex issues raised by the incorporation of RESs into LFC methodologies. The preceding literature has not fully addressed the complications presented by the intermittent and unpredictable nature of RESs, such solar and wind power systems. This work aims to make a substantial contribution by presenting a Flatness-based ADRC approach specifically to address the uncertainties resulting from the intermittent RESs, accommodating load disturbances, un-modeling dynamics, and parameter uncertainties. A modified version of the beluga whale optimization technique, called enhanced beluga whale optimization (EBWO), is used to adjust the controller parameters [37]. A summary of the paper contribution is provided as;

- The integration of the EBWO with FADRC has been presented for multi-area PSs, including thermal power plant and RESs like PV and Wind turbine.
- Beluga whale optimization incorporated with particle swarm optimization is studied to broaden the search range and enhance the likelihood of attaining the optimal solution between the exploration and exploitation phases.
- The suggested FADRC robustness and sensitivity analysis are assessed by taking into account the uncertainties in the model parameters, load demand, wind speed, and solar irradiation.

The structure of the paper is: in section II presents the system components and their mathematical models using transfer functions. Section III discusses the mathematical modeling of the proposed FADRC for the system. Sections IV explains the tuning algorithm for the controller parameters, followed by analyzing the simulation results in section V. Lastly, the conclusion is given in Section VI.

II. MODELING OF POWER SYSTEM

Figure 1 depicts a two-area PS comprising of a thermal generation plant combined with a wind farm in the first area, while the second area is a photovoltaic generation [23]. The overall power deviations in the system under study can be described as:

$$\begin{cases} \Delta P_{total_1} = \Delta P_{th} + \Delta P_W - \Delta P_{D1} + \Delta P_{tie} \\ \Delta P_{total_2} = \Delta P_{PV} - \Delta P_{D2} - \Delta P_{tie} \end{cases} \quad (1)$$

In (1), ΔP_{PV}, ΔP_W, ΔP_{th}, and ΔP_{tie} represent the deviations in power output for the solar, wind, thermal plants, and tie-line power. ΔP_{D1} and ΔP_{D2} correspond to the perturbation in the required load for area 1 and 2, respectively. The APPENDIX contains the system design parameters.

A. MODELING OF THERMAL SYSTEM CONFIGURATION

Within this section, a single generator featuring a reheated turbine is investigated. As shown in Fig. 1, this system

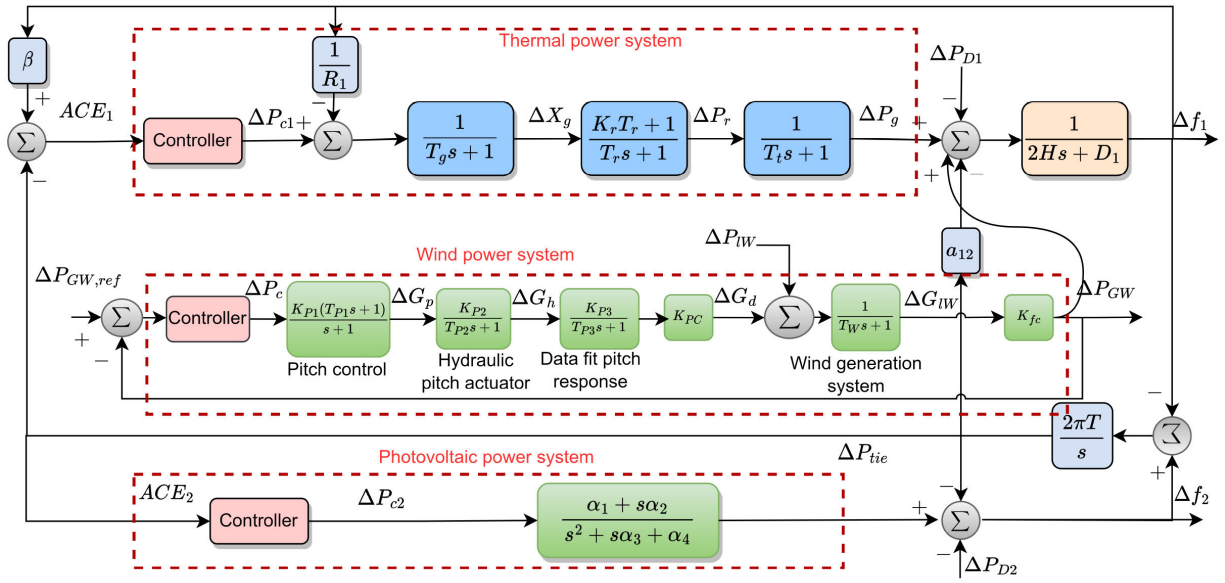

FIGURE 1. Block diagram based on transfer function for a two-area power system.

is used to demonstrate the effectiveness of the suggested strategy. Typically, PSs with a reheated turbine encompasses the subsequent components, represented in the s domain as follow [18], [23].

$$G_g(s) = \frac{1}{T_g(s)+1}$$
$$G_t(s) = \frac{1}{T_t(s)+1}$$
$$G_r(s) = \frac{1+K_rT_r(s)}{T_r(s)+1}$$
$$G_p(s) = \frac{1}{2H(s)+D}$$

where $G_g(s)$, $G_t(s)$, $G_r(s)$, $G_p(s)$ represents the governor, turbine, re-heater and machine, respectively. Area control error(ACE) for area-1 can be expressed as

$$\begin{cases} \Delta P_{tie}(s) & = \dfrac{2\pi T_{12}}{s}(\Delta f_2(s) - \Delta f_1(s)) \\ ACE_1(s) & = B\Delta f_2(s) - \Delta P_{tie} \end{cases} \tag{2}$$

B. MODELING OF WIND SYSTEM CONFIGURATION

Wind Modeling shown in Fig. 1 comprised of different parts [23] which is presented in s domain as follows:

$$\Delta P_c(s) = \frac{K_{p1}(1+sT_{p1})}{1+s} \tag{3}$$

where ΔP_c is th pitch control, K_{p1}, and T_{p1} is the gain and time constant respectively. The ΔG_p is known as the hydraulic pitch actuator defined as

$$\Delta G_p(s) = \frac{K_{p2}}{1+sT_{p2}} \tag{4}$$

where K_{p2}, T_{p2} is the gain and time constant for hydraulic pitch actuator. Where ΔG_H represents the data pitch response presented as

$$\Delta G_H(s) = \frac{K_{p3}}{1+sT_{p3}} \tag{5}$$

where K_{p3} and T_{p3} is the gain and time constant correspondingly. The wind generation part can be expressed as

$$\Delta G_D(s) = \frac{1}{1+sT_w} \tag{6}$$

The output wind power deviation can be expressed as

$$\Delta P_{GW} = K_{fc}G_{1w}(s), \tag{7}$$

and the parameter K_{fc} represent the fluid coupling gain, where K_{pc} is blade characteristic.

C. MODELING OF PHOTOVOLTAIC SYSTEM CONFIGURATION

In area 2, the PV system comprises its all component in a single transfer function such as a PV panel, inverter, filter, and maximum power point tracking (MPPT) [7], [18] [23] is modeled below:

$$G_{PV}(s) = \frac{\alpha_1 + s\alpha_2}{s^2 + \alpha_3 s + \alpha_4} \tag{8}$$

In (8), α_2 represents the PV system gain, α_1 corresponds to the negative zero value in the transfer function, and α_3 as well as α_4 represents the negative pole values [23]. In contrast to the thermal power system, the area control error (ACE_2) in the PV generation area is designed to primarily focus on tie-line power error. This is determined by the intrinsic properties of PV systems, which do not have a direct impact on frequency regulation in the grid because the performance of the PV system is significantly impacted by solar irradiance and temperature variations. Thus, ACE_2 exhibiting an input

for the controller in this particular area is ΔP_{tie}, expressed as follow [23].

$$ACE_1 = \Delta P_{tie} = \frac{2\pi T_{12}}{s}(\Delta f_2 - \Delta f_1) \tag{9}$$

III. FLATNESS-BASED ADRC

Considering an nth-order system with time-varying coefficients along with uncertainties is presented as:

$$\begin{cases} \dot{x}_1 = x_2 \\ \dot{x}_2 = x_3 \\ \vdots \\ \dot{x}_n = -a_{n-1}x_n - a_{n-2}x_{n-1} - \cdots - a_1x_2 - a_0x_1 \\ +b_m u^m + \cdots + b_0 u + f(x_1, \ldots, x_n, u, \ldots, u^m, d) \\ y = x_1 \end{cases} \tag{10}$$

where y is the output, u is the control input, $x = [x_1, x_2, \ldots, x_n]^T$ is the state vector, d is the external disturbance, and $f(x_1, \ldots, x_n, u, \ldots, u^m, d)$ is the total disturbance incorporating the unknown input disturbances and internal dynamics. The set of parameters $a = [a_1, \ldots, a_n]$ are the coefficients.

For the system considered to be flat, there should be a unique output known as flat output denoted by y, and express system variables as a function of y [38] and its finite time derivatives, modelled as:

$$y^n + \sum_{i=0}^{n-1} a_i y^{(i)} = bu + f(t) \tag{11}$$

where $f(t)(y^0, \ldots, y^{(i)}, u, d)$ considered as the total disturbance, comprised of the output and its derivatives $y^{(i)}$, $i = n-1$, control input u, and the external disturbances $d(t)$.

To estimate the total disturbances, it is requisite to design an ESO depending on output variable $y(t)$ and control input $u(t)$ as presented [34]:

$$\begin{cases} \dot{y_0} = y_1 + \lambda_n(e_0) \\ \dot{y_1} = y_2 + \lambda_{n-1}(e_0) \\ \vdots \\ \dot{y_{n-1}} = bu - \sum_{i=0}^{3} a_i y_i + z + \lambda_1(e_0) \\ z = \lambda_0(e_0) \end{cases} \tag{12}$$

where $e_0 = y - y_0$, which is referred to as the redundant estimated output error. This error component effectively fulfills the subsequent perturbed linear dynamics

$$e_0^{(n)} + \lambda_{n-1}e_0^{(n-1)} + \cdots + \lambda_1 \dot{e}_0 + \lambda_0 e_0 = \dot{f}(t) \tag{13}$$

The design parameter set $\lambda_0, \lambda_1, \ldots, \lambda_n - 1$ needs to be adjusted with respect to the following characteristic polynomial:

$$a(s) = s^{(n)} + \lambda_{n-1}s^{(n-1)} + \cdots + \lambda_1 s + \lambda_0 \tag{14}$$

which is a Hurwitz polynomial. To compensate for the estimated perturbed dynamics and for a smooth trajectory tracking task such as $y \to y^*(t)$, $y^*(t)$represents the desired objective, which is achieved by the feedback controller given as

$$u = \frac{1}{b}\left[(y^*(t))^{(n)} - z + \sum_{i=0}^{n-1} a_i y_i - \sum_{i=0}^{n-1} \kappa_i (y_i - (y^*(t))^{(i)})\right]. \tag{15}$$

In (15), $\kappa_i, i = 0, 1, \ldots, n$ are constant coefficients that are deliberately selected to transform the corresponding polynomial into a Hurwitz polynomial [34].

$$q(s) = s^{(n)} + \kappa_{n-1}s^{(n-1)} + \cdots + \kappa_1 s + \kappa_0. \tag{16}$$

A. FADRC CONTROLLER FOR THERMAL SYSTEM

The state space representation for a reheated turbine shown in Fig. 1 is expressed as

$$\begin{cases} \dot{x_1} &= -\frac{D}{H}x_1 + \frac{1}{H}x_2 - \frac{1}{H}(d(t) + P_{tie}(t)) \\ \dot{x_2} &= -\frac{1}{T_t}x_2 + \frac{1}{T_t}x_3 \\ \dot{x_3} &= -\frac{1}{T_r}x_3 + \frac{T_g - T_r K_r}{T_r T_g}x_4 - \frac{K_r}{T_g R}x_1 + \frac{K_r}{T_g}u \\ \dot{x_4} &= -\frac{1}{T_g}x_4 - \frac{1}{T_g R}x_1 + \frac{1}{T_g}u. \end{cases} \tag{17}$$

Here x_1 represents the deviation of frequency Δf, x_2, x_3 and x_4 represents the ΔP_g, ΔP_r and ΔX_g respectively. By observing the (1), the flat output is represented by the frequency deviation $\xi = \Delta f$. Therefore, each variable in the perturbed model needs to be represented as a differential equation in terms of ξ.

$$\begin{aligned} x_2 &= D\xi + H\dot{\xi} + d(t) + P_{tie}(t) \\ x_3 &= D\xi + (DT_t + H)\dot{\xi} + HT_t\ddot{\xi} + T_t(\dot{d}(t) + \dot{P}_{tie}) \\ &\quad + d(t) + P_{tie}(t) \\ x_4 &= \left(\rho D + \frac{\Xi k_r}{T_g R}\right)\xi + (\Xi D + \rho DT_t + \rho H)\dot{\xi} \\ &\quad + (\Xi DT_t + \Xi H + \rho HT_t)\ddot{\xi} + \Xi HT_t\dddot{\xi} \\ &\quad + \Xi T_t(\ddot{d}(t) + \ddot{P}_{tie}(t)) + (\Xi + \rho T_t)(\dot{d}(t) + \dot{P}_{tie}(t)) \\ &\quad + \rho(d(t) + P_{tie}(t)) \\ u &= \frac{1}{\beta}\Bigg\{\left(\rho D + \frac{\Xi k_r}{T_g R} + \frac{1}{R}\right)\xi + \Bigg(\rho T_g D + \Xi D + \rho DT_t \\ &\quad + \rho H + \frac{\Xi K_r}{R}\Bigg)\dot{\xi} + \Bigg(\Xi T_g D + \rho DT_g T_t + \Xi DT_t + \rho T_g H \\ &\quad + \Xi H + \rho HT_t\Bigg)\ddot{\xi} + \Bigg(\Xi DT_t T_g + \Xi T_g H + \rho HT_t T_g \\ &\quad + \Xi HT_t\Bigg)\dddot{\xi} + \Xi HT_t T_g\ddddot{\xi} - \frac{K_r \Xi}{T_g}\dot{u} \\ &\quad + \Xi T_g T_t(\dddot{d}(t) + \dddot{P}_{tie}(t)) + \big(\Xi T_g + \rho T_g T_t \\ &\quad + \Xi T_t\big)\big(\ddot{d}(t) + \ddot{P}_{tie}(t)\big)\big(\Xi + \rho T_t + \rho T_g\big)\big(\dot{d}(t) + \dot{P}_{tie}(t)\big) \\ &\quad + \rho(d(t) + P_{tie}(t))\Bigg\} \end{aligned} \tag{18}$$

where $\Xi = \frac{T_r T_g}{T_g - K_r T_r}$, $\rho = \frac{T_g}{T_g - K_r T_r}$, $\beta = \frac{T_g - K_r T_r - T_g T_r K_r}{T_g - K r T_r}$

$$\dddot{\xi} = -\gamma_4 \dddot{\xi} - \gamma_3 \ddot{\xi} - \gamma_2 \dot{\xi} - \gamma_1 \xi + \beta_0 u - \omega(t)$$

where

$$\begin{aligned}\omega(t) = {} & \frac{1}{H} \dddot{f}_d(t) + \left(\frac{1}{T_t H} + \frac{1}{T_r H} + \frac{1}{T_g H}\right) \ddot{f}_d(t) \\ & + \left(\frac{1}{T_r T_t H} + \frac{1}{T_t T_g H} + \frac{1}{T_r T_g H}\right) \dot{f}_d(t) \\ & + \frac{1}{T_r T_g T_t H} f_d(t) + \frac{Kr}{H T_t T_g^2} \dot{u} \end{aligned} \tag{19}$$

$$\begin{cases} \gamma_1 &= \dfrac{D}{H T_t T_g T_r} + \dfrac{K_r}{H T_t T_g^2 R} + \dfrac{T_g - T_r K_r}{H T_t T_r T_g^2 R} \\ \gamma_2 &= \dfrac{K_r}{H T_t T_g R} + \dfrac{D}{H T_t T_r + H T_t T_g + T_r T_g H} + \dfrac{1}{T_r T_t T_g} \\ \gamma_3 &= \dfrac{D}{H T_t + H T_r + H T_g} + \dfrac{1}{T_g T_r + T_t T_g + T_t T_r} \\ \gamma_4 &= \dfrac{D}{H} + \dfrac{1}{T_r + T_t + T_g} \\ \beta_0 &= \dfrac{H T_g^2 T_r (T_t - T_r K_r) - K_r T_r}{H T_t T_g^2 - T_r} \end{cases} \tag{20}$$

where $f_d(t) = d(t) + P_{tie}(t)$. However, the following system is considered to be invariant in terms of system parameters. Where the process nominal parameters can be computed by (20). Considering the uncertainty in the nominal parameter, the controlled process can be rewritten by including the total disturbance

$$\dddot{\xi} = -\gamma_4 \dddot{\xi} - \gamma_3 \ddot{\xi} - \gamma_2 \dot{\xi} - \gamma_1 \xi + \beta u - f(t) \tag{21}$$

where the total disturbance, $f(t)$, is represented as follows:

$$\begin{aligned} f(t) = {} & e_{\gamma 4} \dddot{\xi} + e_{\gamma 3} \ddot{\xi} + e_{\gamma 2} \dot{\xi} + e_{\gamma 1} \xi \\ & + (\beta - \beta^*) u + \omega(t) \end{aligned} \tag{22}$$

where $e_\gamma = \gamma_i - \gamma_i^*$, $i = 0, 1, 2, 3$, which defines the error in the system parameters and γ_i^* is the nominal parameter value. Assume that

$$\xi_1 = \xi, \xi_2 = \dot{\xi}, \xi_3 = \ddot{\xi}, \xi_4 = \dddot{\xi}, \xi_5 = f, \tag{23}$$

hence the process modal (21) can be represented as

$$\begin{cases} \dot{\xi_1} &= \xi_2 \\ \dot{\xi_2} &= \xi_3 \\ \dot{\xi_3} &= \xi_4 \\ \dot{\xi_4} &= u + \xi_5 \\ \dot{\xi_5} &= f. \end{cases} \tag{24}$$

The tracking goal that follows is developed in order to obtain the process estimated value of the output, its limited-time derivatives, and overall disturbances $f(t)$:

$$\dot{\xi_1}^* \to \xi_2^*, \dot{\xi_2}^* \to \xi_3^*, \dot{\xi_3}^* \to \xi_4^*, \dot{\xi_4}^* \to \xi_5, \xi_5 \to \dot{f}(t) \tag{25}$$

where $\xi_1^*, \xi_2^*, \xi_3^*, \xi_4^*$ are the approximations of $\xi^*, \dot{\xi}^*, \ddot{\xi}^*, \cdots$. In order, to track the system state and estimate the disturbances an ESO is designed as

$$\begin{cases} e_{r1} = (\xi_1 - z_1) \\ \dot{z_1} = z_2 + \lambda_4 e_{r1} \\ \dot{z_2} = z_3 + \lambda_3 e_{r1} \\ \dot{z_3} = z_4 + \lambda_2 e_{r1} \\ \dot{z_4} = \beta u + \lambda_1 e_{r1} + z_5 \\ \dot{z_5} = \lambda_0 e_{r1} \end{cases} \tag{26}$$

where the design parameters $\{\lambda_4, \lambda_3, \lambda_2, \lambda_1, \lambda_0\}$ of the observer are chosen by bandwidth parameterization method [27]. And z_2, z_3, z_4, z_5 are the approximated value of $\xi_2, \xi_3, \xi_4, \xi_5$. Based on the appropriate approximation, sum of the all perturbations $f(t)$ with help of suggested ESO, in accordance with the idea of flatness, a feedback control law can be expressed as

$$\begin{cases} u = \dfrac{1}{\beta}(\gamma_4 \xi_4^* + \gamma_3 \xi_3^* + \gamma_2 \xi_2^* + \gamma_1 \xi_1^* + v - z_5) \\ v = (\xi^*)^{(4)} - \kappa_4 e_{c4} - \kappa_3 e_{c3} - \kappa_2 e_{c2} - \kappa_1 e_{c1} \end{cases} \tag{27}$$

where $e_{ci} = \xi_i^* - z_i$ and $\kappa_1, \kappa_2, \kappa_3, \kappa_4$ are the controller gains need to be optimized to get the desired output trajectory. The controller gains can be specified by governing the characteristic polynomial with all the poles in the left half of the complex plane. The characteristic polynomial corresponds to the Hurwitz polynomial as follows:

$$P(s) = s^4 + \kappa_3 s^3 + \kappa_2 s^2 + \kappa_1 s + \kappa_0 = (s^2 + 2\zeta_c \omega_c s + \omega_c^2)^2$$

where ω_c and ζ_c are the controller bandwidth and damping coefficient respectively. The value of ζ_c is chosen between 0 and 1. the gains of the controller can be computed by $\kappa_3 = 4\zeta_c \omega_c, \kappa_2 = 4\zeta_c^2 \omega_c^2 + \omega_c^2, \kappa_1 = 4\zeta_c \omega_c^3, \kappa_0 = \omega_c^4$. The above procedure has been followed in the next sections by converting the system into a differential flatness problem and then designing an ADRC controller to control the process output.

B. FADRC CONTROLLER FOR WIND SYSTEM

The wind turbine's output power is managed through pitch control, which adjusts the blade angle to match changing wind speeds and maintain optimal performance. The pitch controller utilizes the wind turbine's output power as feedback. Modeling the wind farm system as shown in 1, which can be mathematically represented as

$$\begin{cases} y = K_{fc} x_1 \\ \dot{x_1} = -\dfrac{x_1}{T_w} + \dfrac{K_{pc}}{T_w} x_2 + d(t) \\ \dot{x_2} = -\dfrac{x_2}{T_{p3}} + \dfrac{K_{p3}}{T_{p3}} x_3 \\ \dot{x_3} = -\dfrac{x_3}{T_{p2}} + \dfrac{K_{p2}}{T_{p2}} x_4 \\ \dot{x_4} = -x_4 + K_{p1} T_{p1} \dot{u} + K_{p1} u \end{cases} \tag{28}$$

where, $\Delta P_{GW} = y$, $x_1 = G_{lw}$, $x_2 = G_d$, $x_3 = G_h$, and $x_4 = G_p$. The system presented in (31) is flat with output $F = y = \Delta P_{GW}$, where the system variables can be represented in terms of F and its derivatives. The system unperturbed input to flat output representation can be written as follows:

$$\begin{aligned}
x_1 &= \frac{F}{K_{fc}} \\
x_2 &= \frac{T_w}{K_{pc}K_{fc}}\dot{F} + \frac{1}{K_{pc}K_{fc}}F + \frac{T_w}{K_{pc}K_{fc}}d(t) \\
x_3 &= \frac{T_{p3}T_w}{K_{p3}K_{pc}K_{fc}}\ddot{F} + \frac{T_{p3}+T_w}{K_{p3}K_{pc}K_{fc}}\dot{F} + \frac{1}{K_{p3}K_{pc}K_{fc}}F \\
&\quad - \frac{T_wT_{p3}}{K_{p3}K_{pc}}\dot{d}(t) - \frac{T_w}{K_{p3}K_{pc}}d(t) \\
x_4 &= \frac{T_{p3}T_{p2}T_w}{\varphi}\dddot{F} + \frac{T_{p3}+T_w-T_{p3}T_w}{\varphi}\ddot{F} \\
&\quad + \frac{T_{p2}-T_{p3}+T_w}{\varphi}\dot{F} + \frac{1}{\varphi}F - \frac{T_wT_{p3}T_{p2}}{K_{p2}K_{p3}K_{pc}}\ddot{d}(t) \\
&\quad + \frac{T_wT_{p2}-T_wT_{p3}}{K_{p2}K_{p3}K_{pc}}\dot{d}(t) - \frac{T_w}{K_{p2}K_{p3}K_{pc}}d(t) \\
u &= \frac{T_{p3}T_{p2}T_w}{\varphi K_{p1}}\ddddot{F} + \left(\frac{T_{p3}T_{p2}+T_{p2}T_w+T_{p3}T_w}{\varphi K_{p1}}\right.\\
&\quad \left. + \frac{T_{p3}T_{p2}T_w}{\varphi K_{p1}}\right)\dddot{F} + \left(\frac{T_{p2}+T_{p3}+T_w+T_{p2}T_{p3}}{\varphi K_{p1}}\right.\\
&\quad \left. + \frac{T_{p2}T_w+T_{p3}T_w}{\varphi K_{p1}}\right)\ddot{F} + \frac{T_{p2}+T_{p3}+T_w+1}{\varphi K_{p1}}\dot{F} \\
&\quad + \frac{1}{\varphi K_{p1}}F - T_{p1}\dot{u}
\end{aligned} \tag{29}$$

where $\varphi = K_{p3}K_{p2}K_{pc}K_{fc}$. P_{lW} represents the unknown input disturbance, hence, (31) can be rewritten as:

$$\dddot{F} + \gamma_3\ddot{F} + \gamma_2\ddot{F} + \gamma_1\dot{F} + \gamma_0 F = \beta u - \eta(t) \tag{30}$$

where

$$\begin{cases}
\gamma_3 = \dfrac{1}{T_w} + \dfrac{1}{T_{p3}} + \dfrac{1}{T_{p2}} + 1 \\
\gamma_2 = \dfrac{1}{T_{p3}T_w} + \dfrac{1}{T_{p2}T_w} + \dfrac{1}{T_{p2}T_{p3}} + \dfrac{1}{T_w} + \dfrac{1}{T_{p3}} + \dfrac{1}{T_{p2}} \\
\gamma_1 = \dfrac{1}{T_{p3}T_w} + \dfrac{1}{T_{p2}T_w} + \dfrac{1}{T_{p2}T_{p3}} + \dfrac{1}{T_wT_{p3}T_{p2}} \\
\gamma_0 = \dfrac{1}{T_wT_{p3}T_{p2}} \\
\eta(t) = K_{fc}\dddot{d}(t) + K_{fc}\left(\dfrac{1}{T_p3} + \dfrac{1}{T_p2} + 1\right)\ddot{d}(t) \\
+K_{fc}\left(\dfrac{1}{T_p3} + \dfrac{1}{T_p2} + \dfrac{1}{T_{p3}T_{p2}}\right)\dot{d}(t) + \dfrac{K_{fc}}{T_{p3}T_{p2}}d(t)
\end{cases} \tag{31}$$

To accurately estimate the output F and limited-time derivatives combined with the disturbances $\eta(t)$, a tracking aim is designed as by considering the reference trajectory $r^* = F - F^*$,

$$\dot{F_1^*} \to F_2^*, \dot{F_2^*} \to F_3^*, \dot{F_3^*} \to F_3^*, \dot{F_4^*} \to F_4^*, \dot{F}_5 \to \eta \tag{32}$$

where $F_1^*, F_2^*, F_3^*, F_4^*$ are the approximated values of $F^*, \dot{F}^*, \ddot{F}^*, \dddot{F}^*$. To optimally track the system state and estimate the disturbances an ESO is designed as

$$\begin{cases}
e_w = (F_1 - z_1) \\
\dot{z_1} = F_1 + \lambda_4(e_w) \\
\dot{z_2} = F_2 + \lambda_3(e_w) \\
\dot{z_3} = F_3 + \lambda_2 e_w) \\
\dot{z_4} = \beta u_{eq} + \lambda_1(e_w) + z \\
\dot{z} = \lambda_0(e_w)
\end{cases} \tag{33}$$

The parameters $\lambda_4, \cdot, \lambda_0$ are the observer parameters. In the end, a feedback control law is designed as

$$\begin{cases}
u = \dfrac{1}{\beta}(\gamma_3 F_4 + \gamma_2 F_3 + \gamma_1 F_2 + \gamma_0 F_1 + v - z) \\
v = (F^*)^{(4)} - \kappa_4 e_{wc4} - \kappa_2 e_{wc3} - \kappa_2 e_{wc2} - \kappa_1 e_{wc1}
\end{cases} \tag{34}$$

where $e_{wci} = z_1 - F_1^*$.

C. FADRC CONTROLLER FOR PHOTOVOLTAIC SYSTEM

The PV system represented in (8) can be rewritten as

$$\ddot{y} = -\alpha_4\dot{y} - \alpha_3 y + \alpha_2 u + \alpha_1\dot{u}. \tag{35}$$

Here $x_1 = y$, $x_2 = \dot{y}$, and $\begin{pmatrix} x_1 \\ x_2 \end{pmatrix}$ Therefore, $x_2 = \dot{x_1}$, $\dot{x_2} = -\alpha_4 x_2 - \alpha_3 x_1 + \alpha_2 u + \alpha_1\dot{u}$. Hence $u = f(y)$, therefore

$$\begin{cases}
x_2 &= x_1 \\
\dot{x_2} &= -\alpha_4\dot{x_2} - \alpha_3 x_1 + \alpha_2 f(u) + \alpha_1 f(\dot{u})
\end{cases} \tag{36}$$

By solving the differential equation in terms of $f(y)$, $u = f(y)$ and $\dot{u} = f(\dot{y})$ is a flat system that can be represented in terms of input to flat output as

$$\ddot{F} = -d\dot{F} - cF + \beta u + f(t) \tag{37}$$

where $f(t)$ is the total disturbance including unknown external disturbance, tie-line power deviation, and modal uncertainties. To obtain the process estimated value of the F, and its limited-time derivatives including the disturbances $f(t)$ for a perturbed system, an ESO is given

$$\begin{cases}
e_{pv} &= F - F_0 \\
\dot{F}_0 &= F_1 + \lambda_2(e_{pv}) \\
\dot{F}_1 &= \beta u + \lambda_1(e_{pv}) + z \\
\dot{z} &= \lambda_0(e_{pv})
\end{cases} \tag{38}$$

following the feedback control law is designed as follows

$$\begin{cases}
u = \dfrac{1}{\beta}(\gamma_1 F_1 + \gamma_0 F_0 + v - z) \\
v = (F^*)'' - \kappa_1(F_1 - (F^*)' - \kappa_0(F_0 - F^*)
\end{cases}$$

IV. EBWO ALGORITHM FOR CONTROLLER PARAMETERS TUNING

A. CONVENTIONAL BELUGA WHALE OPTIMIZATION

The Beluga Whale Optimization (BWO) method is a novel optimization technique inspired by the coordinated actions of Beluga whales (BWs) during various activities such as hunting, swimming, and engaging in whale falls [37], [39]. Found in groups of 2 to 25 individuals, Beluga whales exhibit social predator behavior within their natural environment. These groups collaborate in hunting, swimming, and information sharing to obtain a wide variety of food. The BWO algorithm like other algorithms initiates with the initialization step. Then incorporates the exploitation and exploration phases followed by whale fall behaviors of BWs. To mathematically model the BWO, the beluga whales are randomly initialized with each whale is considered as a solution and will be updated accordingly. The beluga whales positions are presented in a matrix (X) of a size ($n \times d$) presented below:

$$\chi = \begin{pmatrix} x_{1,1} & \cdots & x_{i,d} \\ \vdots & \ddots & \vdots \\ x_{1,n} & \cdots & x_{n,d} \end{pmatrix} \tag{39}$$

with the corresponding fitness values of each beluga whales are listed as:

$$F_\chi = \begin{pmatrix} f(x_{1,1}, \cdots, x_{i,d}) \\ \vdots \\ f(x_{n,1}, \cdots, x_{n,d}) \end{pmatrix} \tag{40}$$

The exploration phase of the BWO replicates the swimming behavior of two pairs of closely swimming Beluga whales, either synchronized or moving randomly. It can be represented as follows:

$$\begin{cases} \chi_{i,j}^{T+1} = \chi_{i,p_j}^{T} + \left(\chi_{r,p_1}^{T} - \chi_{i,p_j}^{T}\right) \\ \qquad (1 + r_1)\sin(2\pi r_2), j = even \\ \chi_{i,j}^{T+1} = \chi_{i,p_j}^{T} + \left(\chi_{r,p_1}^{T} - \chi_{i,p_j}^{T}\right) \\ \qquad (1 + r_1)\cos(2\pi r_2), j = odd \end{cases} \tag{41}$$

in which T denotes the current iteration and $\chi_{i,j}^{T+1}$ indicates the updated location for the ith beluga whale along the jth dimension. $\chi_{r,p1}^{T}$ represents a random selected beluga whale, r_1 and r_2 are randomly selected within [0, 1] range.

The exploitation phase of the BWO is inspired by the preying behavior of the beluga whale in which they share the information to hunt, guided by the best solution of the BW. To improve the convergence ability of the algorithm, a Levy flight strategy has been utilized in the exploitation phase which is mathematically expressed as:

$$\chi_i^{T+1} = r_3\chi_{best}^{T} - r_4\chi_i^{T} + C_1 \cdot L_F \cdot (\chi_r^{T} - \chi_i^{T}) \tag{42}$$

χ_r^T and χ_i^T are the current positions of random and ith BW respectively, while r_3 and r_4 are random numbers ranging from 0 to 1, and χ_{best}^T is the best location of a beluga whale. In (42) C_1 is the random step size that calculates the intensity of the Levy flight expressed as

$$C_1 = 2r_4(1 - T/T_{max}) \tag{43}$$

where L_F describes the Leavy flight function and is expressed as

$$L_F = 0.05 \times \frac{u \times \sigma}{|v|^{1/\beta}} \tag{44}$$

where

$$\sigma = \left(\frac{\Gamma(1+\beta) \times \sin(\pi\beta/2)}{\Gamma((1+\beta)/2) \times \beta \times 2^{(\beta-1)/2}}\right)^{1/\beta} \tag{45}$$

here u and v are the random numbers, while β is the constant factor with a value of 1.5. The transition of BW focus from exploration to exploitation is influenced by the equilibrium factor $B_f = B_0(1 - T/2T_{max})$, B_0 is a random value chosen from the interval [0,1]. The algorithm is in the state of exploration if $B_f > 0.5$, and will shift to exploitation as soon as the $B_f \leq 0.5$. The increasing number of iterations T and reduction in the range of B_f from [0,1] to [0, 0.5], increase the likelihood of the exploitation stage.

During the whale fall phase, Beluga whales (BWs) are vulnerable to predation by killer whales and human activities while migrating and foraging. In this phase, deceased BWs sink to the seafloor, and to maintain consistent population size, their positions are updated using the following as

$$\chi_i^{T+1} = r_5\chi_i^{T} - r_6\chi_r^{T} + r_7\chi_{step} \tag{46}$$

where r_5, r_6 and r_7 are the random numbers in range $0 \leq r_5, r_6, r_7 \geq 1$. χ_{step} is the step size of the whale fall which can be expressed as:

$$\chi_{step} = (u_b - l_b)exp(-C_2T/T_max) \tag{47}$$

where l_b and u_b are the boundaries of the variables and C_2 is a time-varying factor determined by the population size and the probability of whale fall as follows:

$$C_2 = 2W_f \times n \tag{48}$$

where whale fall is denoted by W_f which is a linear function and can be calculated as:

$$W_f = 0.1 - 0.05T/T_{max}. \tag{49}$$

B. ENHANCED BWO

The conventional Beluga Whale Optimization (BWO) method is enhanced by incorporating Particle Swarm Optimization (PSO) [40] during the whale fall phase. PSO is renowned for its robust exploration capabilities. Leveraging the swarm's collective movement, whales can navigate through a variety of regions within the search space, consequently enhancing the chances of discovering superior solutions. Moreover, the exploitation aspect of PSO, where particles gravitate towards the best-found positions, aids BWO in converging towards promising areas. This characteristic entails global information sharing among particles

through their respective best-match positions. By capitalizing on this information sharing, whales can communicate their optimal positions, thereby influencing the movement of their counterparts which ultimately drives better convergence. The velocity and position components of the PSO algorithm are expressed as follows

$$V_{ij}(t+1) = \omega \cdot V_{ij}(t) + c_1 \cdot \Upsilon_1 \cdot (P_{b_{ij}}(t) - \chi_{ij}(t)) + c_2 \cdot \Upsilon_2 \cdot (G_{b_j}(t) - \chi_{ij}(t)) \quad (50)$$

$$\chi_{ij}(t+1) = \chi_{ij}(t) + V_{ij}(t+1) \quad (51)$$

where $V_{ij}(t)$ represents the velocity of BWs i in dimension j at time t, ω is the inertia weight, $P_{b_{ij}}(t)$ is the personal best position of BW i in dimension j at time t, $\chi_{ij}(t)$ is the current position of BW i in dimension j at time t. The flowchart and pseudo code can be found in Fig.2 and Algorithm 1, respectively. Application of the proposed EBWO utilized for tuning the parameters of the controller shown in Fig. 1.

C. IMPLEMENTATION AND COMPARISON OF PROPOSED EBWO WITH OTHER METAHEURISTIC ALGORITHMS

To initiate the optimization, initial parametric values are as follows: population size of $N = 25$, a maximum iteration limit of $M = 300$, and Dimension $D = 30$. Providing a clear understanding of how the EBWO algorithm operates, the procedural steps are depicted in a flowchart shown in Figure 2. This flowchart offers a detailed overview of how the optimization process is executed using the EBWO algorithm.

To evaluate the performance improvement achieved by the Enhanced Beluga Whale Optimization(EBWO) algorithm, compared with several recently developed optimization algorithms, including the Bat algorithm [41], Firefly algorithm [42], Particle Swarm Optimization [40], and the traditional Beluga Whale Optimization [37]. EBWO algorithm is evaluated on five different benchmarks [37] including unimodal and multimodal functions, as detailed in Table 1. The analysis included tracking the minimum fitness value obtained with the EBWO algorithm and the convergence curve for the competitive algorithms shown in Figure3 and 4. The performance of these algorithms has been evaluated, and the results were analyzed using statistical metrics, including mean, mode, median, and standard deviation (STD) given in Table 2. Overall performance of the EBWO algorithm demonstrates superior performance as compared to other optimization techniques across all benchmark problems. The superior performance, as reflected in the statistical data, underscores the effectiveness and robustness of the EBWO algorithm in obtaining optimal solutions for the given functions.

Therefore, to use the EBWO algorithm for optimizing the proposed FADRC for the purpose of LFC, an Integral Time Absolute Error (ITAE) serves as the performance index to achieve the optimal gain values(controller bandwidth(ω_c) and observer bandwidth(ω_o)). ITAE is frequently employed in LFC studies [31], providing a robust settling time. As a result, minimizing ITAE is essential. Mathematically, ITAE

Algorithm 1 algorithm

Input: Initialize the population with algorithmic parameters (population size, maximum iteration)
Output: The best solution

```
Evaluate fitness values based on initial population and obtain the best solution (P*)
while T ≤ T_max do
    Compute Whale fall W_f by Eq (49) and B_f
    for each beluga X_i do
        if B_f > 0.5 then
            // Exploration phase
            Generate random values for p(j = 1, 2, ..., d)
            Choose a beluga whale X_r randomly
            Update the new position using Eq (41)
        else
            if B_f ≤ 0.5 then
                // Exploitation phase
                Update C_1 and compute L_f
                Update the new position using Eq (42)
            end
        end
    end
    Check the boundaries and Evaluate fitness
    for each beluga X_i do
        // Whale fall phase
        if B_f ≤ 0.5 then
            Update C_2 and compute X_step
            if case = PSO then
                Update the new position using Eq (51)
            else
                Update the new position using Eq (46)
            end
            Check the boundaries and Evaluate fitness
        end
    end
    Find the current best solution
    T = T + 1;
end
Output the best solution
```

is expressed as

$$J = ITAE = \int_0^{t_{sim}} (\sum_{n=1}^{i} \Delta f_i + \sum_{n=1}^{j} \Delta P_{tie,j}) t dt. \quad (52)$$

The value of J must be minimized to improve the dynamic response of the system, the ITAE comprised of the response of deviation in frequency (Δf_1, Δf_2) in area 1 and area 2,and the tie-line power deviation $\Delta P_{tie,j}$. The optimum controller gains are obtained within the defined bounds for the PV, thermal system, and wind turbine controller separately given as

$$\omega_{o,min} \leq \omega_o \leq \omega_{o,max}$$
$$\omega_{c,min} \leq \omega_c \leq \omega_{c,max} \quad (53)$$

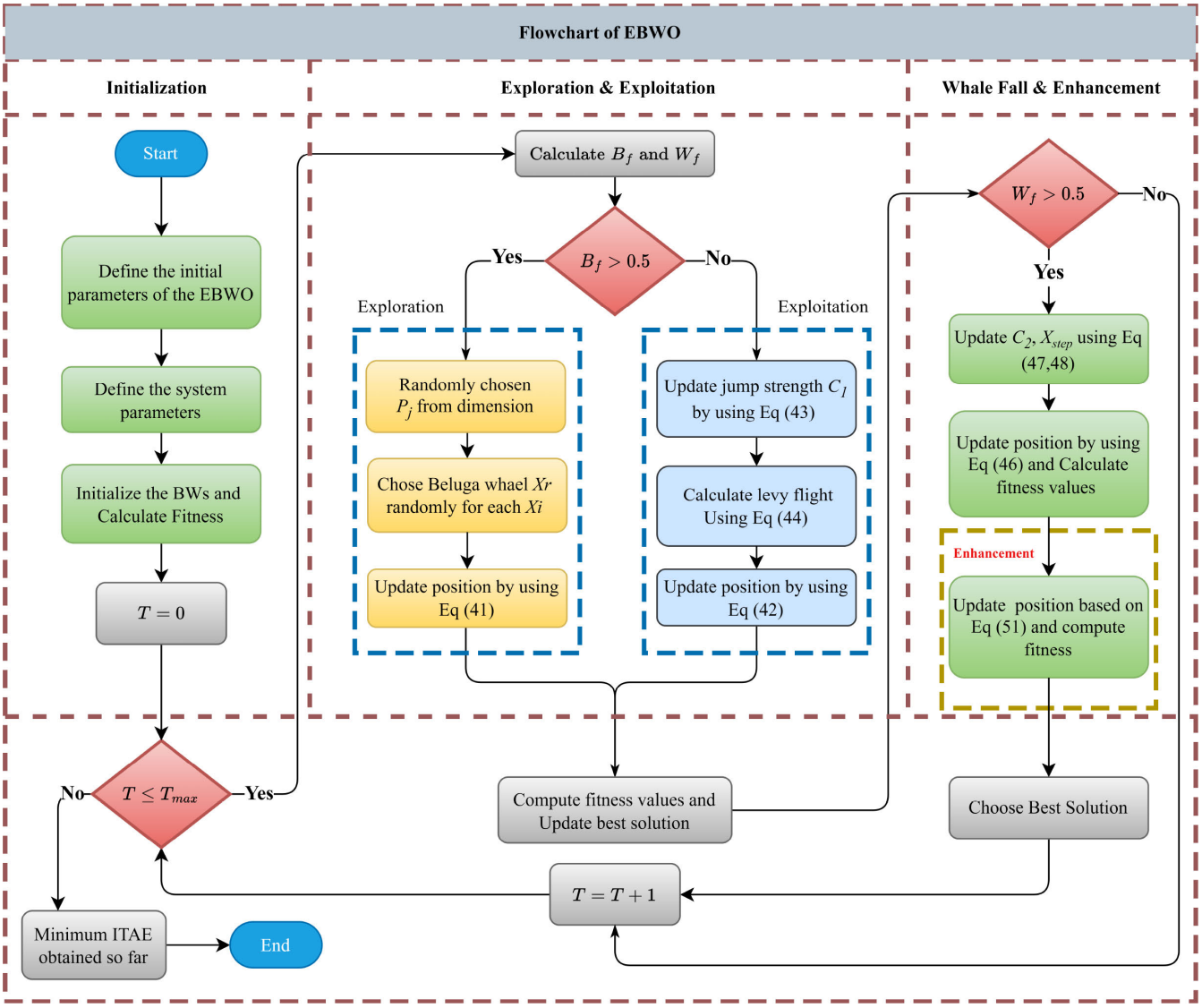

FIGURE 2. Flow chart of the EBWO algorithm for tuning controllers parameters.

TABLE 1. Details of the test benchmark problem.

Name	Function	Range	f_{min}
Sphere	$F_1 = \sum_{i=1}^{D} x_i^2$	[-100, 100]	9.332e-162
Schwefel's 1.2	$F_2 = \sum_{i=1}^{D} \left(\sum_{i=1}^{D} x_j\right)^2$	[-100, 100]	4.593e-171
Rosenbrock	$F_3 = \sum_{i=1}^{D} \left[100\left(x_{i+1} - x_i^2\right)^2 + \left(x^i - 1\right)^2\right]$	[-30, 30]	0.01019
Step	$F_4 = \sum_{i=1}^{D} \left(x_i + 0.5\right)^2$	[-100, 100]	1.208e-5
Ackley	$F_5 = -20\exp\left(-0.2\sqrt{\frac{\left(\sum_{i=1}^{D} x_i^2\right)}{D}}\right) - \exp\left(\frac{\left(\sum_{i=1}^{D} cos(2\pi x_i)\right)}{D}\right) + 20 + e$	[-32, -32]	8.882e-16

V. SIMULATION RESULTS

MATLAB/SIMULINK 2019b is used to build and simulate the model shown in Fig.1. In this study, the system parameters used for simulations are given in Appendix. The optimal gains of PID, LADRC, and FADRC were obtained by using the designed EBWO. Firstly, a two-area PS is taken into consideration for analysis, the first area is a thermal power plant with a wind penetration whilst the second area is a PV plant as presented [7], [23]. Secondly, the system is extended to four areas. The superiority, robustness, and sensitivity of the proposed EBWO-tuned FADRC controller are being analysed by taking into account the subsequent scenarios.

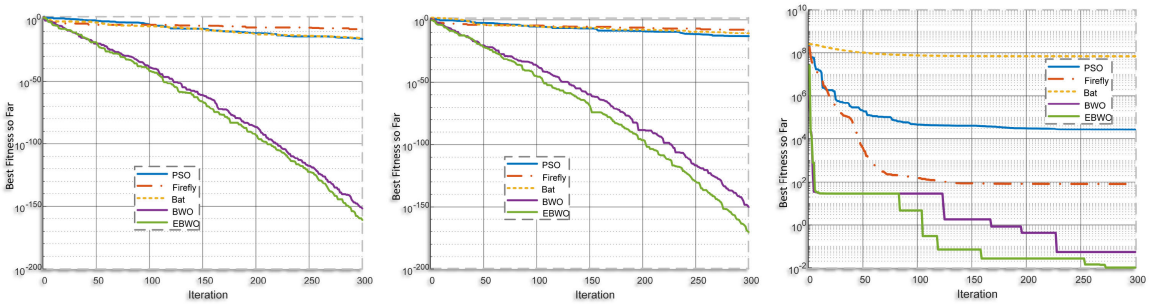

(a) F_1 (b) F_2 (c) F_3

FIGURE 3. Convergence curve for function F_1, F_2, and F_3.

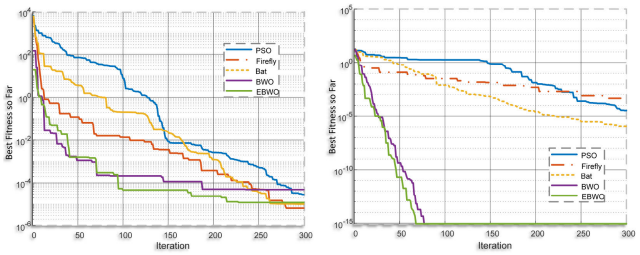

(a) F_1 (b) F_2

FIGURE 4. Convergence curve for function F_4 and F_5.

TABLE 2. Results of the test benchmark functions for compared algorithms.

Function	Algorithm	Mean	Median	Mode	STD
F_1	PSO	0.448	1.259e-08	6.578e-15	2.999
	Firefly	0.07005	3.475e-06	1.788e-05	1.062
	BAT	0.04836	3.393e-09	5.712e-06	0.5168
	BWO	0.006793	6.626e-62	1.468e-20	0.1096
	EBWO	0.02843	2.94e-67	7.238e-84	0.3184
F_2	PSO	0.3025	2.48e-07	3.443e-07	2.682
	Firefly	1.927	3.353e-06	7.062e-07	1.145
	BAT	1.927	7.02e-07	1.547e-08	7.78
	BWO	0.02039	2.162e-60	3.846e-89	0.3012
	EBWO	0.003738	1.539e-69	5.307e-75	0.03979
F_3	PSO	2.039e+06	4.088e+04	2.7e+04	1.39e+07
	Firefly	1.47e+06	85.42	82	1.193e+07
	BAT	8.744e+07	6.99e+07	6.835e+07	3.953e+07
	BWO	3307	1.806	28.7	5.489e+04
	EBWO	8.561e+04	0.07187	0.02773	1.481e+06
F_4	PSO	113.4	0.008514	0.007227	469.6
	Firefly	26.72	0.003539	0.01591	289.9
	BAT	38.48	0.02223	0.03224	379
	BWO	1.649	0.0001164	0.00004884	14.67
	EBWO	0.2547	0.00004641	0.00001208	1.974
F_5	PSO	1.708	0.7699	1.859	2.73
	Firefly	0.2024	0.01378	0.001903	1.203
	BAT	0.7287	0.0006236	3.039e-06	2.215
	BWO	0.1271	8.882e-16	8.882e-16	1.193
	EBWO	0.03948	8.882e-16	8.882e-16	0.3502

1) Comparison of the proposed scheme with optimized controller
2) Impact of high load demand
3) Sensitivity analysis
4) Fluctuation in load and RESs
5) Photovoltaic system downtime
6) Four area PS

A. COMPARISON OF THE PROPOSED SCHEME WITH OPTIMIZED CONTROLLERS

In this scenario, a load deviation of 1% in area-1 and 2 with a step time of 5s. Comparisons have been made with other controllers optimized by different optimization algorithms such as Firefly optimized PI [7], PSO-based LADRC [11], Bat algorithm-based LADRC [31] and the EBWO based PID and LADRC. Fig. 5 illustrates the responses of competing controllers in the multi-area PS. Subsequently, Fig. 5a and Fig. 5b represents the frequency variation for both areas. Fig. 5c shows the tie-line power deviation. The analysis particularly centres on both tie-line power and frequency deviations. The dynamic responses indicate the effectiveness of the proposed EBWO-optimized FADRC controller. It shows enhanced dynamic performance in contrast to alternative controllers with minimum overshoot and settling time. The competitive controllers are evaluated based on ITAE, settling time(s), and overshoot(p.u.) as tabulated in Table 3 and 4. Based on this comparison, it is evident that the proposed EBWO-tuned FADRC controller yields significantly less settling time (s), overshoot, and ITAE results. In area 1, FADRC obtains a settling time of 10.5821(s) and an overshoot of 0.0011(p.u.) which is very small as compared to the competitive controllers. Also in area 2, the FADRC controller demonstrates the smallest settling time and overshoot, measuring at 10.7677 (s) and 0.0104 (p.u.) respectively, while exhibiting an ITAE of 552.0376. The overall performance of the proposed EBWO-based FADRC is more robust and effective in its dynamic response and performance indices.

TABLE 3. Performance indices of competitive controllers in Area 1.

Controller	Δf_1		
	Settling time(s)	Overshoot(p.u.)	ITAE
FA-PID	30	0.0176	7486
PSO-LADRC	23.4038	0.0114	1102.7
BAT-LADRC	22.9077	0.0043	609.6877
EBWO-PID	28.4410	0.0176	4968.9
EBWO-LADRC	23.2025	0.0031	287.2218
EBWO-FADRC	10.5821	0.0011	193.6188

B. IMPACT OF HIGH LOAD DEMAND

In this case, the system is examined by subjecting it to successive step changes in load demand in the thermal power system, while the WT and PV system remains unchanged. The first step change is 0.1pu and the second change is 0.4 at the 20s, Table 5 and 6 shows the settling time, overshoot,

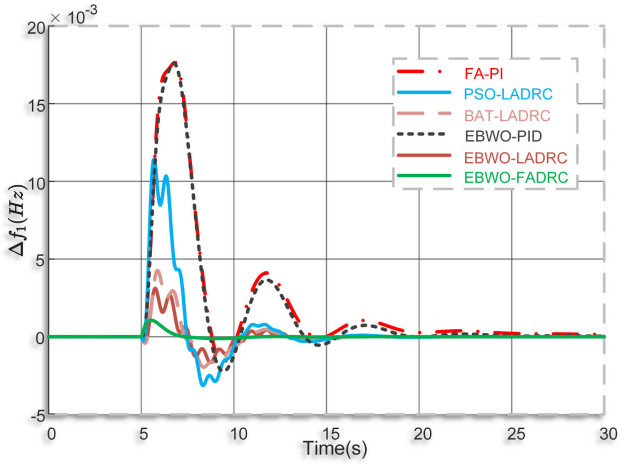

(a)

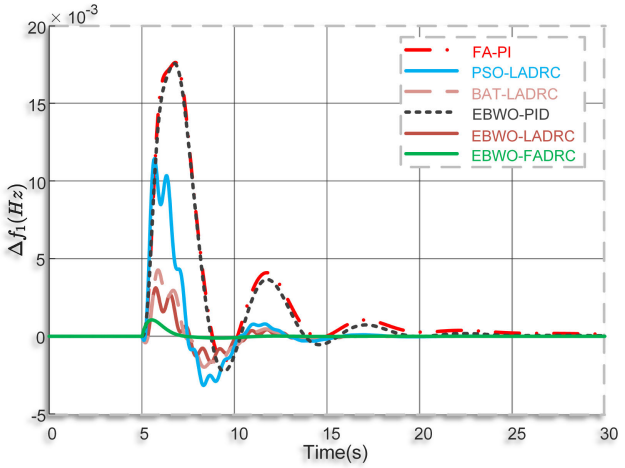

(b)

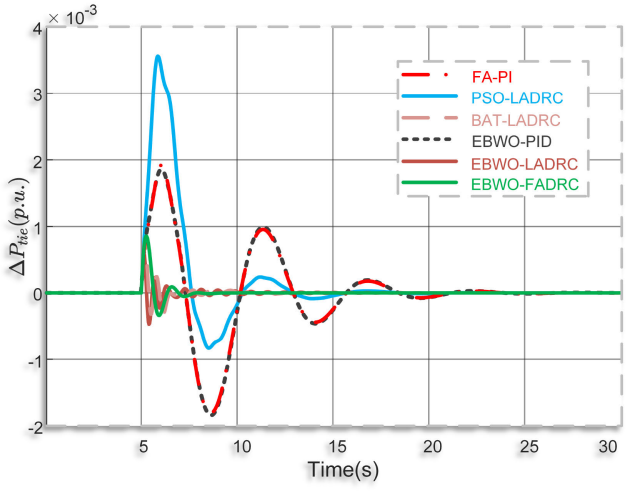

(c)

FIGURE 5. Responses of the competing controllers, (a) and (b) is Frequency deviation in Area 1 and 2 respectively, (c) tie-line power deviation.

and ITAE indices of the controllers. Results illustrated the lowest values for the proposed controller FADRC indices. The dynamic performance is depicted in Fig. 6, Fig. 6a

TABLE 4. Performance indices of competitive controllers in Area 2.

Controller	Δf_2		
	Settling time(s)	Overshoot(p.u.)	ITAE
FA-PID	30	0.0208	8928.80
PSO-LADRC	30	0.0122	1844.1
BAT-LADRC	30	0.0104	990.5231
EBWO-PID	30	0.0206	6809.0
EBWO-LADRC	20.9343	0.0111	757.6267
EBWO-FADRC	10.7677	0.0104	552.0376

TABLE 5. Performance indices of area-1 with high load demand.

Controller	Δf_1		
	Settling time(s)	Overshoot(p.u.)	ITAE
PID	30.3340	0.0246	3.6389e+06
LADRC	29.2782	0.0140	10777
FADRC	23.1215	0.0028	347.8358

TABLE 6. Performance indices of area-2 with high load demand.

Controller	Δf_2		
	Settling time(s)	Overshoot(p.u.)	ITAE
PID	30.8060	0.0211	4.3795e+06
LADRC	32.5912	0.0129	15505
FADRC	23.5322	0.0103	314.6907

and Fig. 6b shows the frequency responses for area 1 and 2, respectively, while Fig. 6c is the tie-line power deviation. The EBWO-based FADRC controller demonstrates robustness and significantly improves the system's damping and settling time characteristics compared to the LADRC and PID controllers.

C. SENSITIVITY ANALYSIS

The sensitivity analysis has been conducted to further examine the scientific validity of the proposed EBWO-based FADRC by measuring its robustness to parameter uncertainties. This addresses a common drawback of competitive methods, where performance deteriorates significantly with even minor model uncertainties and could lead to the deviation of frequency and tie-line power from their nominal values. To, analyze the stability and robustness of the proposed method against the competitive controllers, the parameter values $((0.04 \leq T_g \leq 0.12, 0.15 \leq T_t \leq 0.45, 5 \leq T_r \leq 15, 0.165 \leq T_g \leq 0.495))$, are changed by $\pm 50\%$ from the values listed in Appendix. Firstly, the parameters are changed from their nominal values by $+50\%$ to test the stability of the system, the dynamic response of the proposed controller and the competitive controllers are shown in Fig. 7. Secondly, the system parameters are changes from their nominal values by -50% to further assess the system performance in the presence of uncertainties, and the simulation results are shown in Fig. 8. Overall, results shows that the proposed EBWO-based FADRC indicates stability and robustness against uncertainties, and is more efficient as compared to LADRC and PID. Even when there's uncertainty about the model parameters, there is no need to reset the controller gains. Moreover,

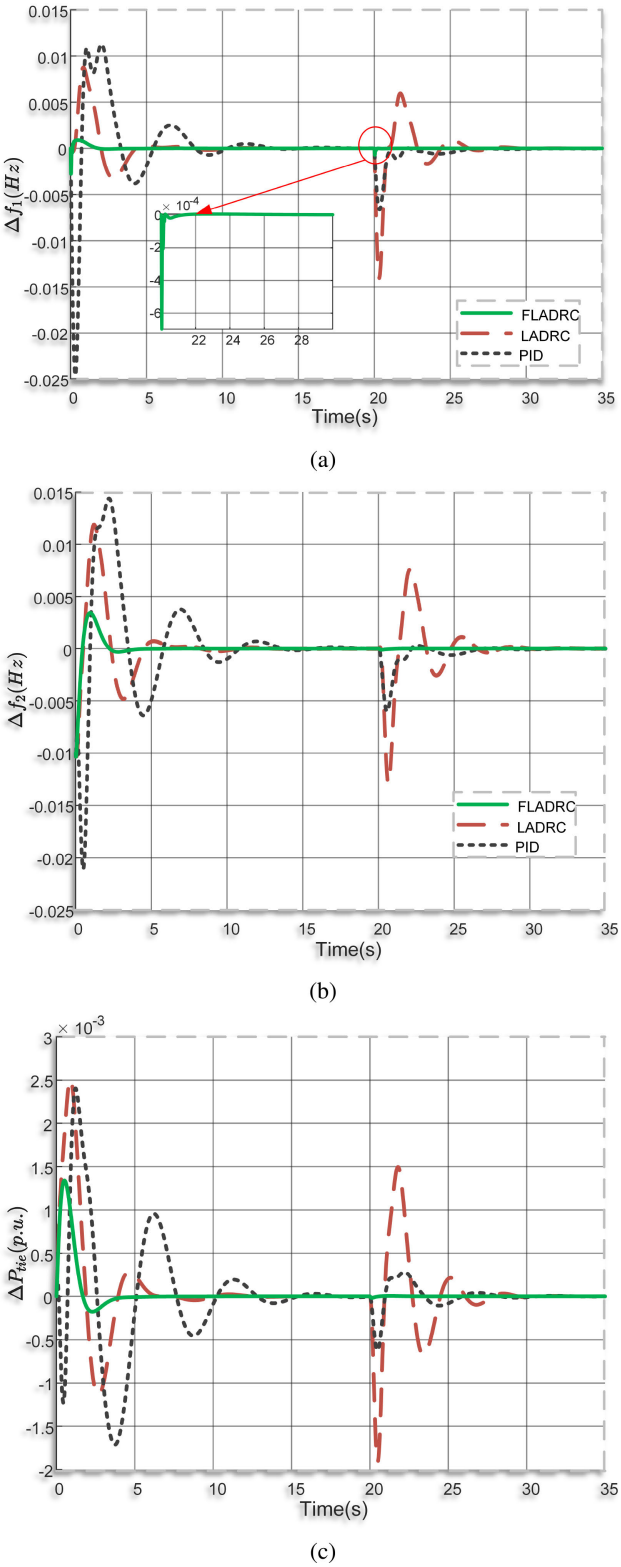

FIGURE 6. Response in the presence of high load demand, (a,b) is the deviation of frequency in area-1 and 2 respectively, (c) tie-line power deviation.

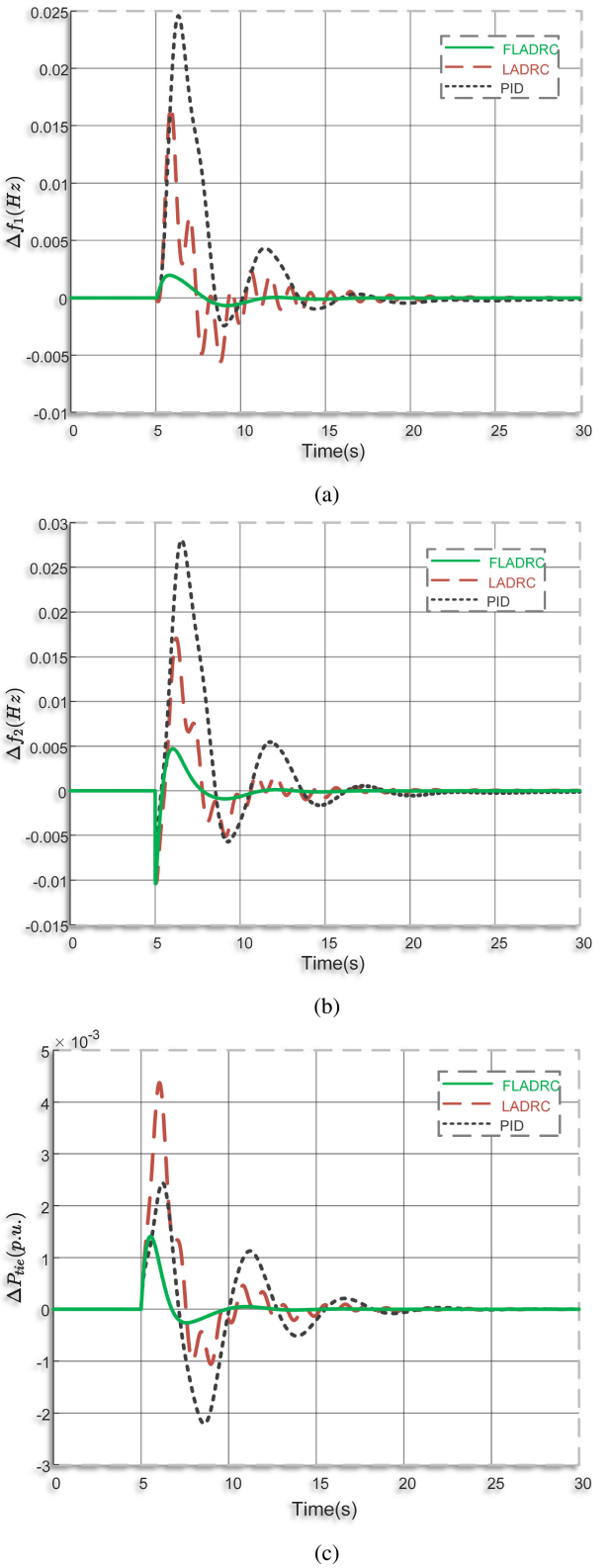

FIGURE 7. Dynamic responses for a +50%, (a,b) is the deviation of frequency in area-1 and 2 respectively, (c) Tie-line power deviation.

a detailed comparison between FADRC, LADRC, and PID is presented in Table 7 and 8 for the key performance indices(settling time(s), overshoot(p.u.), and ITAE) shows the substantial practical benefits of EBWO-based FADRC as the minimum indices have been achieved in the presence of practical parameters uncertainties. Overall results, highlight

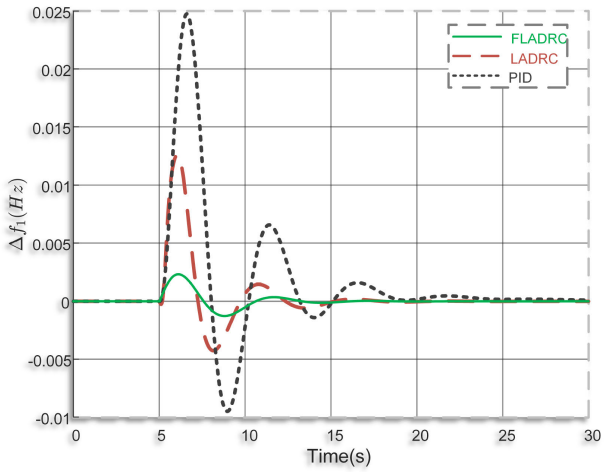

(a)

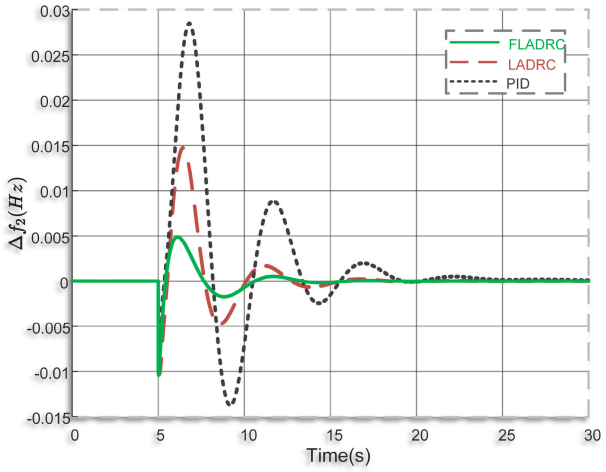

(b)

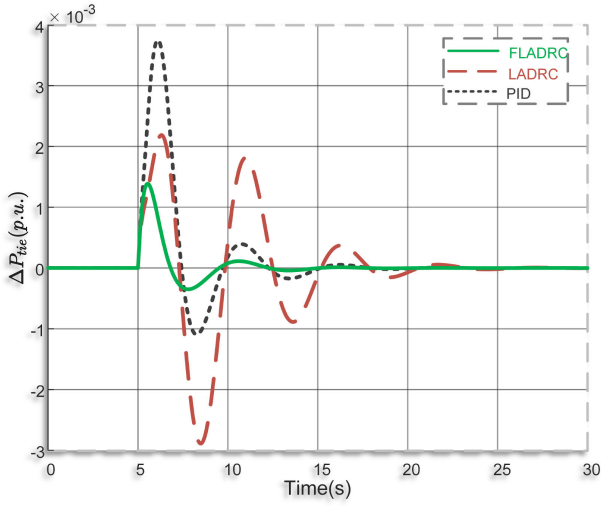

(c)

FIGURE 8. Dynamic responses for a -50%, (a,b) is the deviation of frequency in area-1 and 2 respectively, (c) Tie-line power deviation.

its effectiveness and suitability in real-world scenarios. This comprehensive sensitivity analysis, therefore, not only supports the theoretical validity of EBWO-based FADRC but also emphasizes its practical worth as a robust and efficient control method.

TABLE 7. Performance indices for parameters variation in the range of ±50% in Area 1.

Variations	Controllers	Δf_1		
		Settling time(s)	Overshoot(p.u.)	ITAE
+50%	PID	30	0.0244	5741.5
	LADRC	27.1288	0.0168	2558.4
	FADRC	15.9156	0.0020	637.84
−50%	PID	30	0.0248	9554.8
	LADRC	19.6551	0.0126	1455.5
	FADRC	15.5702	0.0023	1116.3

TABLE 8. Performance indices for parameters variation in the range of ±50% in Area 2.

Variations	Controllers	Δf_1		
		Settling time(s)	Overshoot(p.u.)	ITAE
+50%	PID	30	0.0279	7824
	LADRC	29.7257	0.0171	2495.2
	FADRC	16.0590	0.0104	1133.8
−50%	PID	35	0.0285	12464
	LADRC	22.6084	0.0147	2263.1
	FADRC	17.7237	0.0104	1941

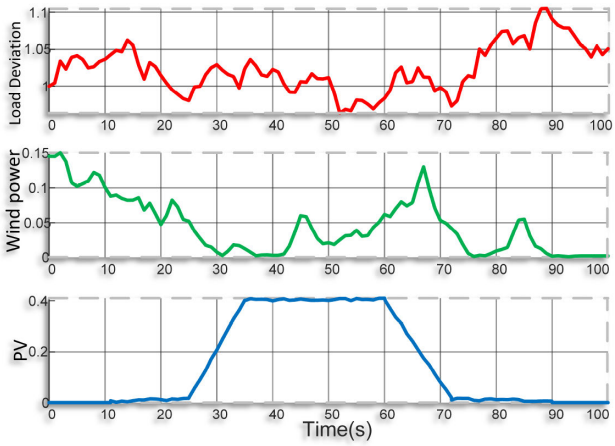

FIGURE 9. (a) Wind power deviation (b)Load power deviation (c) Solar power deviation.

D. FLUCTUATION IN LOAD AND RESS

In this case, the practical uncertainties of wind speed, solar radiation, and load variations have been considered to evaluate the system response. The wind power data is obtained from the [43] for real-time implementation. Solar power fluctuation is designed accordingly given in [44] and load deviation is modeled by using band-limited noise followed by initial input [23]. These deviations in the load, wind, and solar irradiance are shown in Fig. 9, offering a clear depiction of the fluctuating nature of the RESs. Fig. 10 illustrates the results of competing controllers for both frequency and tie-line power deviations in the presence of RESs uncertainties and load deviation. The dynamic results and the subsequent analysis demonstrate the superiority of the proposed FADRC controller. Regardless of notable

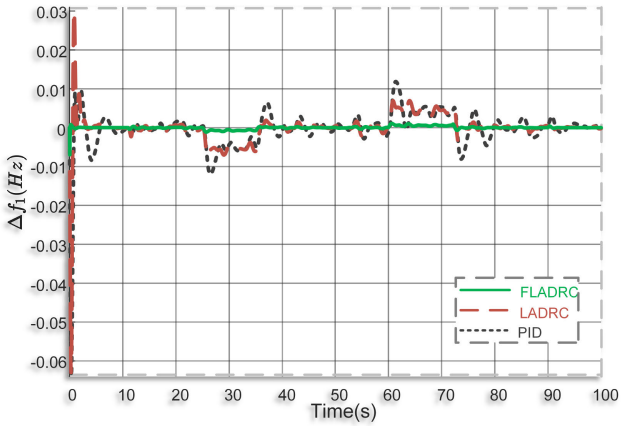

(a)

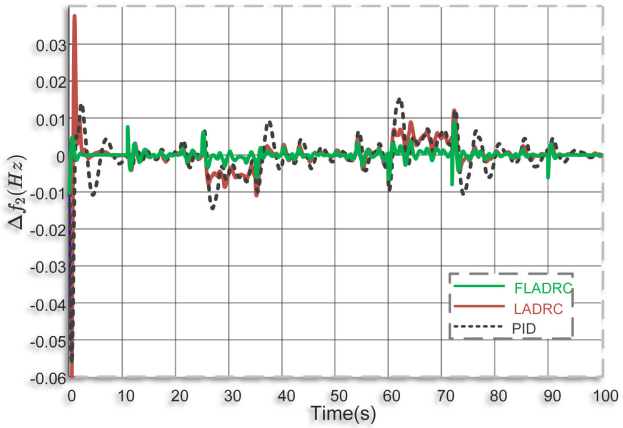

(b)

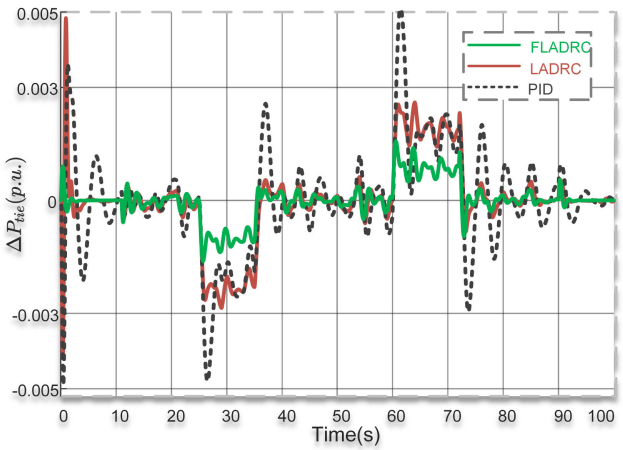

(c)

FIGURE 10. Simulation results in the presence of load, wind, and solar deviation, (a) and (b) is deviation of frequency in Area-1 and 2 respectively,(c) Tie-line power deviation.

fluctuations in RESs and load demands, the system's dynamic performance shows how reliable and effective the suggested FADRC controller is. The frequency change in areas 1 and 2 deviate within the acceptable range, even during instances of substantial load demand as shown in Fig. 10. The system responses exhibit the superiority and efficiency of the

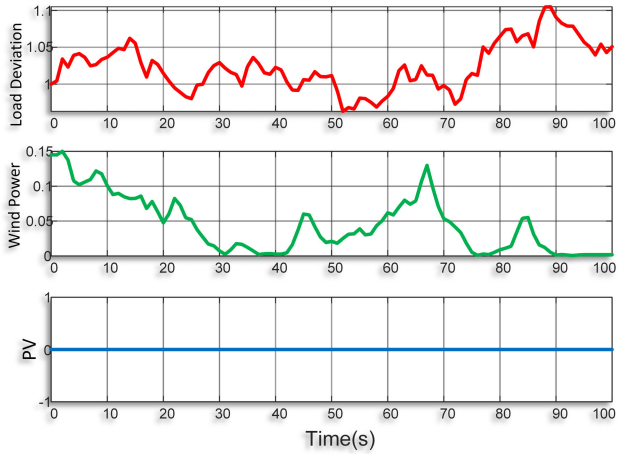

FIGURE 11. Changes in RESs and load.

proposed FADRC controller with EBWO-tuned parameters in facing the practical uncertainties of wind speed, solar irradiance, and load deviations.

E. PHOTOVOLTAIC SYSTEM DOWNTIME

In this simulation scenario, our main objective was to assess the system's reaction to real-world uncertainties in wind speed and load fluctuations, while not considering the influence of photovoltaic (PV) generation. PV sources have downtime especially during the night-time or due to weather conditions as depicted in Fig. 11. During these times the wind and thermal power system will manage to maintain the equilibrium between the load and generation. Figure 12 illustrates the dynamic responses of different controllers concerning both frequency and tie-line power deviations, taking into account uncertainties in wind speed and load variations. The results indicate that the overshoot of the EBWO-based FADRC controller is very small with respect to the competing controllers and always in an acceptable range. Although there is no photovoltaic generation, the analysis demonstrates the robustness and efficacy of the EBWO-based FADRC controller.

F. FOUR-AREA POWER SYSTEM

In this case, the LFC technique based FADRC is utilized on a commonly employed four-area PS [10]. The structure of the system is shown in Fig 13. Each area is comprised of the non-reheated turbine shown in Fig. 14, while the wind power penetrated in area-4.

1) MODELING OF FLATNESS BASED ADRC FOR NON-REHEAT POWER SYSTEM

In the non reheat unit, let $x_1 = \Delta f, x_2 = \Delta P_m, x_3 = \Delta X_G$ and $d = \Delta P_d$, the LFC model is designed as:

$$\dot{x}(t) = Ax(t) + B_1u(t) + B_2d(t) \tag{54}$$

$$y(t) = Cx(t). \tag{55}$$

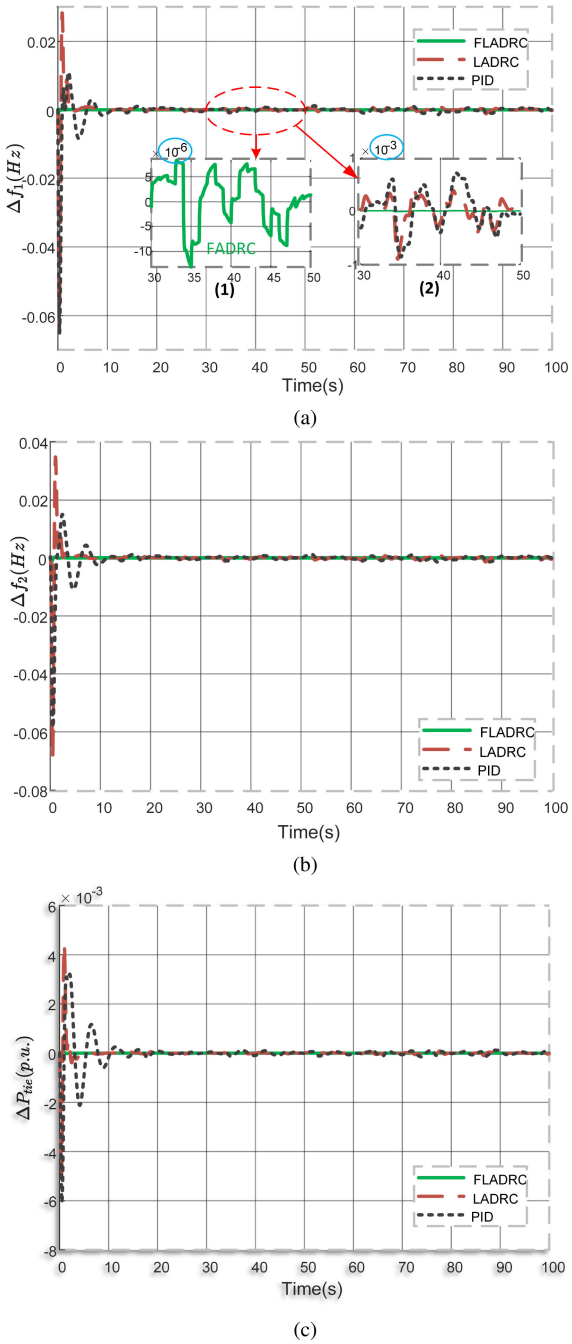

FIGURE 12. Results in the absence of PV (a) and (b)is Frequency deviation in Area 1 and 2 respectively,(c) Tie-line power deviation.

where

$$A = \begin{bmatrix} -\frac{1}{T_p} & \frac{K_p}{T_p} & 0 \\ 0 & -\frac{1}{T_t} & \frac{1}{T_t} \\ \frac{1}{T_g R} & 0 & -\frac{1}{T_g} \end{bmatrix}$$

$$B_1 = \begin{bmatrix} 0 \\ 0 \\ \frac{1}{T_g} \end{bmatrix}, \text{and } B_2 = \begin{bmatrix} \frac{K_p}{T_p} \\ 0 \\ 0 \end{bmatrix} \quad C = \begin{bmatrix} 1 \\ 0 \\ 0 \end{bmatrix}.$$

From the system, it can be observed that the system is flat, all of the variables can be represented as function of flat

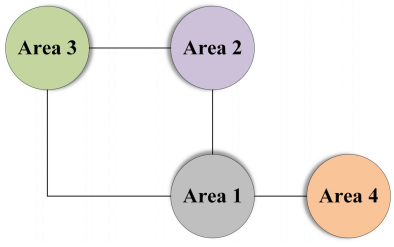

FIGURE 13. Four area structure.

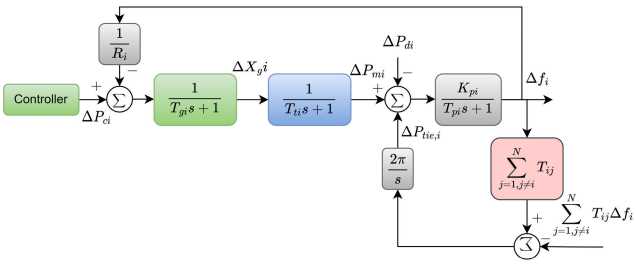

FIGURE 14. Single area non-reheated system.

output $F = y$.

$$\begin{cases} x_2 = \frac{1}{K_p}F + \frac{T_p}{K_p}\dot{F} \\ x_3 = \frac{1}{K_p}F + \frac{T_p + T_t}{K_p}\dot{F} + \frac{T_t T_p}{K_p}\ddot{F} \\ u = \left(\frac{1}{K_p} + \frac{1}{R}\right)F + \left(\frac{T_p}{K_p} + \frac{T_t}{K_p} + \frac{T_g}{K_p}\right)\dot{F} \\ + \left(\frac{T_p T_t}{K_p} + \frac{T_p T_g}{K_p} + \frac{T_t T_g}{K_p}\right)\ddot{F} + \frac{T_t T_p T_g}{K_p}\dddot{F} \end{cases} \tag{56}$$

where $d(t)$ in (54) is the unknown input disturbance, by including the disturbances input to the flat output of the model is expressed as

$$\dddot{F} + \gamma_2\ddot{F} + \gamma_1\dot{F} + \gamma_0 F = bu + \eta(t) \tag{57}$$

where

$$\begin{cases} \gamma_2 = \frac{1}{T_g} + \frac{1}{T_t} + \frac{1}{T_p}, \gamma_1 = \frac{1}{T_g T_t} + \frac{1}{T_p T_g} + \frac{1}{T_p T_t}, \\ \gamma_0 = \frac{K_p + R}{T_g T_p T_t R}, b = \frac{K_p}{T_g T_p T_t} \\ \eta(t) = \frac{K_p}{T_g T_p T_t}d(t) + K_p\left(\frac{T_g + T_p}{T_g T_t T_p}\right)\dot{d}(t) + \frac{K_p}{T_p}\ddot{d}(t). \end{cases} \tag{58}$$

To appropriately estimate the output variable F and its finite time derivatives along with parameters uncertainties considered as a total disturbance, an ESO is designed as given by

$$\begin{cases} e_{nr} = (F - F_0) \\ \dot{F}_0 = F_1 + \lambda_4(e_{nr}) \\ \dot{F}_1 = F_2 + \lambda_3(e_{nr}) \\ \dot{F}_2 = \beta u + z - \sum_{i=0}^{2}\gamma_i F_i + \lambda_1(e_{nr}) \\ \dot{z} = \lambda_0(e_{nr}). \end{cases} \tag{59}$$

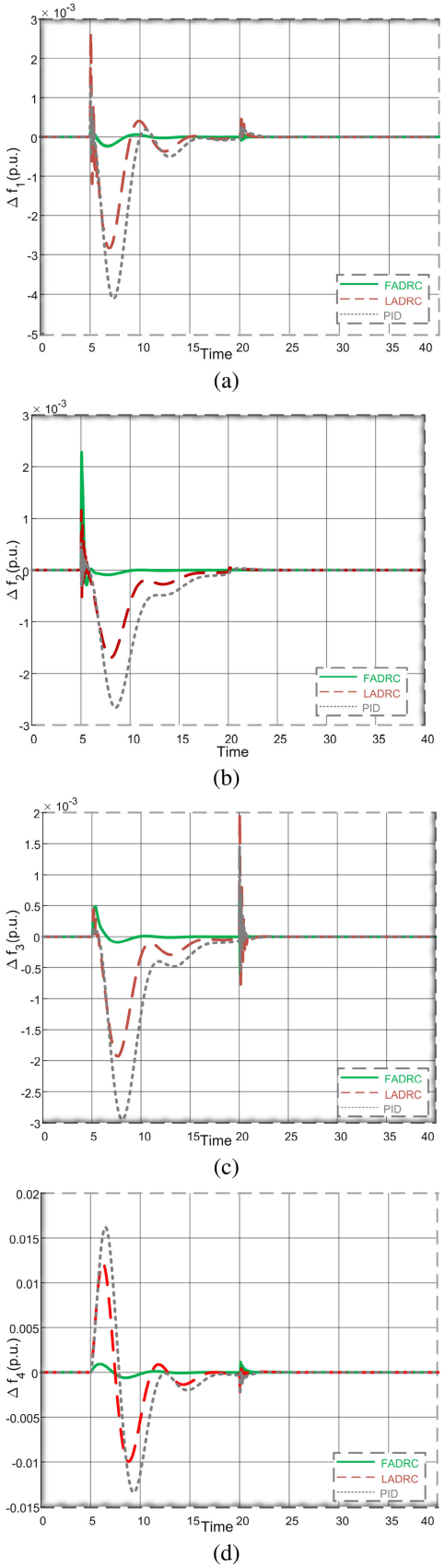

FIGURE 15. Frequency deviation of the four-areas.

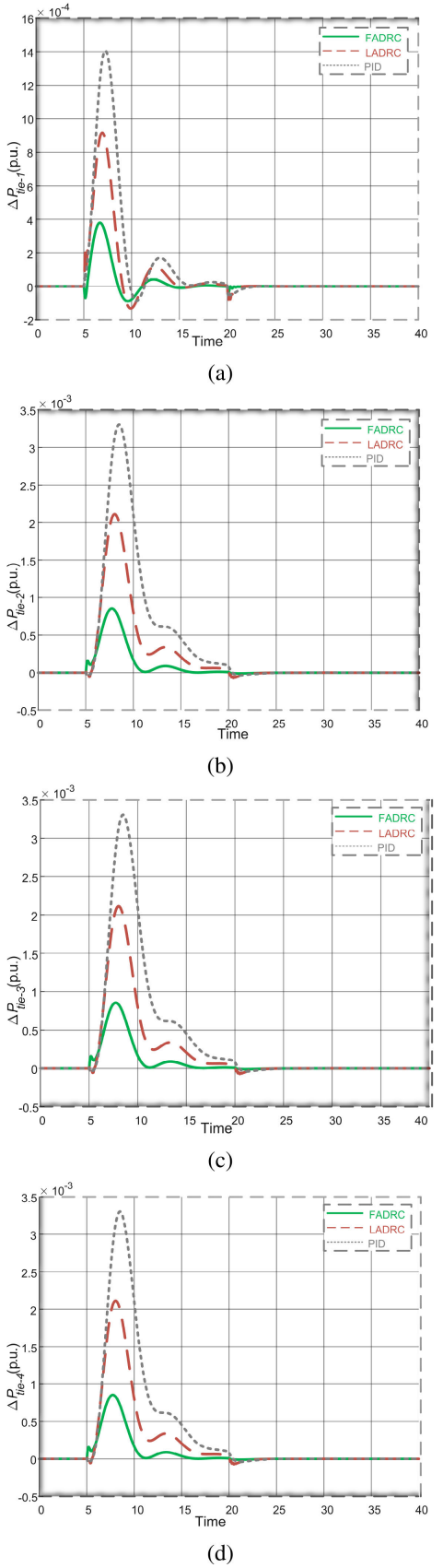

FIGURE 16. Tie-line power deviation of the four-areas.

TABLE 9. Parameters of the non-reheated four-area system.

Area #	T_g	T_t	T_p	K_p
1	0.4	0.08	20	120
2	0.33	0.072	25	112.5
3	0.35	0.07	20	115
4	0.375	0.085	20	120

In (57), $\eta(t)$ is the total disturbance which can be accurately estimated as z in (59), a feedback control law using the idea of flatness as a foundation mathematically expressed as

$$\begin{cases} u = \dfrac{1}{\beta}(\gamma_2 F_2 + \gamma_1 F_1 + \gamma_0 F_0 + v - z) \\ v = (F^*)^{(''')} - \kappa_2(F_2 - (F^*)'') - \kappa_1(F_1 - (F^*)') \\ -\kappa_0(F - F^*) \end{cases} \tag{60}$$

here y^* represents the reference trajectory and $\kappa_2, \kappa_1, \kappa_0$ are the control gains that can be determined by bandwidth parameterization.

2) SIMULATION RESULTS

Considering the model with non reheated turbine and wind power penetration in area 4, and the parameters used are given in Table 9. A load disturbance of 0.01 p.u. has been applied simultaneously to area-1 and 2 at $t = 5s$, with a consecutive step load deviation in area-3 and 4 of 0.01 p.u. at $t = 20s$. Fig.15 shows the frequency deviation in the four-area PS of the competitive controllers.

The suggested LFC scheme, as depicted in Fig 15, demonstrates a significant enhancement in the system frequency as compared to the linear ARRC and PID. Considering the quick response of the suggested LFC scheme, a prompt control measure can be executed whenever there are disturbances. Consequently, even when the governor and generator exhibit slow dynamics, the FADRC expedites the attainment of a stable state for system frequency, resulting in a considerably smaller frequency deviation when compared to the existing controller. Fig 16 demonstrates the variation in tie-line power of the four-areas. Simulation results are evidence that the FADRC effectively reduces the frequency and tie-line power deviation, and achieves faster convergence towards zero deviation.

VI. CONCLUSION

In this paper, a robust Flatness-based Active Disturbance Rejection Control (FADRC) scheme is proposed for LFC, incorporating an Enhanced Beluga Whale Optimization Algorithm. The LFC model encompasses diverse area power systems with renewable resources, including photovoltaic generation and wind turbines. Initially, the system is transformed into a differential flatness model, addressing the complexity of real-world power systems. Then, total disturbances, including tie-line power deviations, load variations, and parameter uncertainties, are considered as lumped disturbances. An extended state observer is developed to approximate and track the overall disturbances in order to effectively handle these disturbances. Finally, a feedback control law is developed to mitigate dynamic errors. To ensure optimal performance, the controller gains are fine-tuned utilizing the enhanced Beluga Whale Optimization Algorithm, resulting in superior control outcomes. The simulation results indicate the optimum settling time of 10.5821s, minimal overshoot(0.0011p.u.), and ITAE(193.6188), with a settling time improvement of 89.41%. Furthermore, in comparison to proportional integral derivative and linear active disturbance rejection control methods, the results demonstrate robustness and efficiency of the suggested controller.

In the future, this research can be extended to include intricate battery storage systems in the absence of photovoltaic cells and address the challenges associated with electrical vehicles. Furthermore, investigating system delays is a remarkable subject that warrants extensive investigation in the ongoing research efforts and extending the current optimization algorithm to a multi-objective optimization algorithm.

APPENDIX

A. PV system parameters:

$\alpha_1 = 900, \alpha_2 = -18, \alpha_3 = 100, \alpha_4 = 50$

B. Thermal power system parameters:

$P_R = 2000$MW(rating), $P_L = 1000$MW(nominal loading); $f = 60$Hz; $R_1 = 2.5$Hz/p.u. MW; $B = 0.425$p.u MW/Hz; $T_g = 0.08$s; $T_t = 0.3$s; $T_r = 10$s; $K_r = 0.33pu$ MW; $K_p = 120$Hz/pu MW; $T_p = 20$s; $2\pi T_{12} = 0.545$p.u.; $a_{12} = -1$.

C. Parameters for wind turbine:

$K_{p1} = 1.25$pu MW; $T_{p1} = 0.6$ s; $K_{p2} = 1$ pu MW; $T_{p2} = 0.041$ s; $K_{pc} = 0.08$; $K_{fc} = 1.494$; $K_{p3} = 1.4$ pu MW; $T_{p3} = 1$ s; $T_w = 4$ s.

REFERENCES

[1] A. Q. Al-Shetwi, M. A. Hannan, K. P. Jern, M. Mansur, and T. M. I. Mahlia, "Grid-connected renewable energy sources: Review of the recent integration requirements and control methods," *J. Cleaner Prod.*, vol. 253, Apr. 2020, Art. no. 119831.

[2] M. H. Saeed, W. Fangzong, B. A. Kalwar, and S. Iqbal, "A review on microgrids' challenges & perspectives," *IEEE Access*, vol. 9, pp. 166502–166517, 2021.

[3] B. Khokhar, S. Dahiya, and K. P. S. Parmar, "A novel hybrid fuzzy PD-TID controller for load frequency control of a standalone microgrid," *Arabian J. Sci. Eng.*, vol. 46, no. 2, pp. 1053–1065, Feb. 2021.

[4] J. Guo, "Application of full order sliding mode control based on different areas power system with load frequency control," *ISA Trans.*, vol. 92, pp. 23–34, Sep. 2019.

[5] G. Panda, S. Panda, and C. Ardil, "Automatic generation control of interconnected power system with generation rate constraints by hybrid neuro fuzzy approach," *Int. J. Elect. Power Energy Syst. Eng.*, vol. 2, no. 1, pp. 13–18, 2009.

[6] A. Khalil, Z. Rajab, A. Alfergani, and O. Mohamed, "The impact of the time delay on the load frequency control system in microgrid with plug-in-electric vehicles," *Sustain. Cities Soc.*, vol. 35, pp. 365–377, Nov. 2017.

[7] S. M. Abd-Elazim and E. S. Ali, "Load frequency controller design of a two-area system composing of PV grid and thermal generator via firefly algorithm," *Neural Comput. Appl.*, vol. 30, no. 2, pp. 607–616, Jul. 2018.

[8] D. Yousri, T. S. Babu, and A. Fathy, "Recent methodology based Harris hawks optimizer for designing load frequency control incorporated in multi-interconnected renewable energy plants," *Sustain. Energy, Grids Netw.*, vol. 22, Jun. 2020, Art. no. 100352.

[9] C. Mu, Y. Tang, and H. He, "Improved sliding mode design for load frequency control of power system integrated an adaptive learning strategy," *IEEE Trans. Ind. Electron.*, vol. 64, no. 8, pp. 6742–6751, Aug. 2017.

[10] K. Liao and Y. Xu, "A robust load frequency control scheme for power systems based on second-order sliding mode and extended disturbance observer," *IEEE Trans. Ind. Informat.*, vol. 14, no. 7, pp. 3076–3086, Jul. 2018.

[11] Y. Tang, Y. Bai, C. Huang, and B. Du, "Linear active disturbance rejection-based load frequency control concerning high penetration of wind energy," *Energy Convers. Manag.*, vol. 95, pp. 259–271, May 2015.

[12] B. Sonker, D. Kumar, and P. Samuel, "Dual loop IMC structure for load frequency control issue of multi-area multi-sources power systems," *Int. J. Elect. Power Energy Syst.*, vol. 112, pp. 476–494, Nov. 2019.

[13] A. Darvish Falehi, "Robust and intelligent type-2 fuzzy fractional-order controller-based automatic generation control to enhance the damping performance of multi-machine power systems," *IETE J. Res.*, vol. 68, no. 4, pp. 2548–2559, 2022.

[14] M. Hannan, S. Y. Tan, A. Q. Al-Shetwi, K. P. Jern, and R. Begum, "Optimized controller for renewable energy sources integration into microgrid: Functions, constraints and suggestions," *J. Cleaner Prod.*, vol. 256, May 2020, Art. no. 120419.

[15] A. Giallanza, M. Porretto, G. L. Puma, and G. Marannano, "A sizing approach for stand-alone hybrid photovoltaic-wind-battery systems: A Sicilian case study," *Journala Cleaner Prod.*, vol. 199, pp. 817–830, Oct. 2018.

[16] M. Ranjan and R. Shankar, "A literature survey on load frequency control considering renewable energy integration in power system: Recent trends and future prospects," *J. Energy Storage*, vol. 45, Jan. 2022, Art. no. 103717.

[17] H. H. Alhelou, N. Nagpal, N. Kassarwani, and P. Siano, "Decentralized optimized integral sliding mode-based load frequency control for interconnected multi-area power systems," *IEEE Access*, vol. 11, pp. 32296–32307, 2023.

[18] P. Dahiya and A. K. Saha, "Frequency regulation of interconnected power system using black widow optimization," *IEEE Access*, vol. 10, pp. 25219–25236, 2022.

[19] A. D. Falehi, "MOBA based design of FOPID-SSSC for load frequency control of interconnected multi-area power systems," *Smart Struct. Syst.*, vol. 22, no. 1, pp. 81–94, 2018.

[20] A. D. Falehi, "Optimal fractional order BELBIC to ameliorate small signal stability of interconnected hybrid power system," *Environ. Prog. Sustain. Energy*, vol. 38, no. 5, p. 13208, Sep. 2019.

[21] T. Mahto and V. Mukherjee, "Fractional order fuzzy PID controller for wind energy-based hybrid power system using quasi-oppositional harmony search algorithm," *IET Gener., Transmiss. Distrib.*, vol. 11, no. 13, pp. 3299–3309, 2017.

[22] D. Tripathy, N. D. Choudhury, and B. Sahu, "A novel cascaded fuzzy PD-PI controller for load frequency study of solar-thermal/wind generator-based interconnected power system using grasshopper optimization algorithm," *Int. J. Elect. Eng. Educ.*, vol. 60, pp. 1801–1818, 2023.

[23] A. A. A. El-Ela, R. A. El-Sehiemy, A. M. Shaheen, and A. E.-G. Diab, "Design of cascaded controller based on coyote optimizer for load frequency control in multi-area power systems with renewable sources," *Control Eng. Pract.*, vol. 121, Apr. 2022, Art. no. 105058.

[24] J. Han, "From PID to active disturbance rejection control," *IEEE Trans. Ind. Electron.*, vol. 56, no. 3, pp. 900–906, Mar. 2009.

[25] D. Sun, "Comments on active disturbance rejection control," *IEEE Trans. Ind. Electron.*, vol. 54, no. 6, pp. 3428–3429, Dec. 2007.

[26] A. Abadi, A. El Amraoui, H. Mekki, and N. Ramdani, "Flatness-based active disturbance rejection control for a wheeled mobile robot subject to slips and external environmental disturbances," *IFAC-PapersOnLine*, vol. 53, no. 2, pp. 9571–9576, 2020.

[27] Z. Gao, "Scaling and bandwidth-parameterization based controller tuning," in *Proc. ACC*, 2003, pp. 4989–4996.

[28] Z. Gao, "On the centrality of disturbance rejection in automatic control," *ISA Trans.*, vol. 53, no. 4, pp. 850–857, Jul. 2014.

[29] W. Tan, Y. Hao, and D. Li, "Load frequency control in deregulated environments via active disturbance rejection," *Int. J. Electr. Power Energy Syst.*, vol. 66, pp. 166–177, Mar. 2015.

[30] Y. Zheng, Z. Chen, Z. Huang, M. Sun, and Q. Sun, "Active disturbance rejection controller for multi-area interconnected power system based on reinforcement learning," *Neurocomputing*, vol. 425, pp. 149–159, Feb. 2021.

[31] S. Ali, G. Yang, and C. Huang, "Performance optimization of linear active disturbance rejection control approach by modified bat inspired algorithm for single area load frequency control concerning high wind power penetration," *ISA Trans.*, vol. 81, pp. 163–176, Oct. 2018.

[32] H. Sira-Ramirez and S. K. Agrawal, *Differentially Flat Systems*. Boca Raton, FL, USA: CRC Press, 2018.

[33] M. Fliess, J. Lévine, P. Martin, and P. Rouchon, "Flatness and defect of non-linear systems: Introductory theory and examples," *Int. J. Control*, vol. 61, no. 6, pp. 1327–1361, Jun. 1995.

[34] C. Huang and H. Sira-Ramírez, "Flatness-based active disturbance rejection control for linear systems with unknown time-varying coefficients," *Int. J. Control*, vol. 88, no. 12, pp. 2578–2587, Dec. 2015.

[35] H. Wang, T. Pan, H. Sira-Ramirez, and Z. Gao, "Flatness-based discrete active disturbance rejection control for the flexible transmission system," *J. Control, Autom. Electr. Syst.*, vol. 32, no. 6, pp. 1746–1757, Dec. 2021.

[36] B. Zhang, J. Li, W. Tan, H. Sira-Ramírez, and Z. Gao, "Estimated flatness-based active disturbance rejection control for load frequency control of power systems," *Electr. Power Compon. Syst.*, vol. 50, nos. 19–20, pp. 1250–1262, 2022.

[37] C. Zhong, G. Li, and Z. Meng, "Beluga whale optimization: A novel nature-inspired metaheuristic algorithm," *Knowl.-Based Syst.*, vol. 251, Sep. 2022, Art. no. 109215.

[38] Y. Xia, M. Lin, J. Zhang, M. Fu, C. Li, S. Li, and Y. Yang, "Trajectory planning and tracking for four-wheel steering vehicle based on differential flatness and active disturbance rejection controller," *Int. J. Adapt. Control Signal Process.*, vol. 35, no. 11, pp. 2214–2244, 2021.

[39] M. H. Hassan, S. Kamel, F. Jurado, M. Ebeed, and M. F. Elnaggar, "Economic load dispatch solution of large-scale power systems using an enhanced Beluga whale optimizer," *Alexandria Eng. J.*, vol. 72, pp. 573–591, Jun. 2023.

[40] J. Kennedy and R. Eberhart, "Particle swarm optimization," in *Proc. Int. Conf. Neural Netw. (ICNN)*, vol. 4, Dec. 1995, pp. 1942–1948.

[41] X. Yang and A. Hossein Gandomi, "Bat algorithm: A novel approach for global engineering optimization," *Eng. Comput.*, vol. 29, no. 5, pp. 464–483, Jul. 2012.

[42] A. H. Gandomi, X.-S. Yang, S. Talatahari, and A. H. Alavi, "Firefly algorithm with chaos," *Commun. Nonlinear Sci. Numer. Simul.*, vol. 18, no. 1, pp. 89–98, Jan. 2013.

[43] Y. Chen and J. Xu, "Solar and wind power data from the Chinese state grid renewable energy generation forecasting competition," *Sci. Data*, vol. 9, no. 1, p. 577, Sep. 2022.

[44] S. Jain and Y. V. Hote, "Generalized active disturbance rejection controller design: Application to hybrid microgrid with communication delay," *Int. J. Elect. Power Energy Syst.*, vol. 132, Nov. 2021, Art. no. 107166.

SHAHZAD ALI received the master's degree in control theory and control engineering from North China Electric Power University, Beijing, China, in 2019. He is currently pursuing the Ph.D. degree in control science and engineering with the Beijing Institute of Technology, Beijing. His research interests include load frequency control, optimization algorithm, machine learning, and active disturbance rejection control.

YUANQING XIA (Fellow, IEEE) received the Ph.D. degree in control theory and control engineering from Beihang University, Beijing, China, in 2001.

He was a Research Fellow in several academic institutions, from 2002 to 2008, including the National University of Singapore and the University of Glamorgan, U.K. Since 2004, he has been with the Beijing Institute of Technology (BIT), China, where he is currently a Full Professor and the Dean of the School of Automation, BIT. He is also the Director of the specialized committee on cloud control and decision of the Chinese Institute of Command and Control (CICC), a member of the Eighth Disciplinary Review Group of the Academic Degrees Committee of the State Council, a member of the Big Data Expert Committee of the Chinese Computer Society, and the Vice-Chairperson of the Internet of Things Working Committee of the Chinese Institute of Instrumentation. He was granted by the National Outstanding Youth Foundation of China, in 2012. He was honored as the Yangtze River Scholar Distinguished Professor, in 2016, and the leading talent of the Chinese Ten Thousand Talents Program. He obtained the Second Award of the Beijing Municipal Science and Technology (No. 1), in 2010 and 2015, the Second National Award for Science and Technology (No. 2), in 2011, the Second Natural Science Award of the Ministry of Education (No. 1), in 2012 and 2017, and the Second Wu Wenjun Artificial Intelligence Award (No. 1), in 2018. He has published 16 monographs in Springer, John Wiley, CRC, and more than 500 articles in international scientific journals and he has been a Highly Cited Scholar, since 2014, by Elsevier. He is a Deputy Editor of the *Journal of Beijing Institute of Technology*, an Associate Editor of *Acta Automatica Sinica*, *International Journal of Automation and Computing*, *Guidance and Navigation*, and *Control Theory and Applications*. More than five of his students have obtained excellent doctoral thesis awards from the Chinese Association of Automation or the Chinese Institute of Command and Control. His research interests include cloud control systems, networked control systems, robust control, and signal processing, active disturbance rejection control, and flight control.

ZOHAIB AHMAD KHAN received the master's degree in control science and engineering from the Beijing Institute of Technology, Beijing, China, in 2017, where he is currently pursuing the Ph.D. degree in control science and engineering. His research interests include machine learning, natural language processing, data mining, knowledge graphs, and AI.

ABID ALI received the B.S. and M.S. degrees in electrical engineering from the University of Management and Technology, Lahore. He is currently pursuing the Ph.D. degree in control science and engineering with the Beijing Institute of Technology, Beijing, China. His research interests include machine learning, power system analysis, voltage stability within power systems, microgrids, energy management systems, and the integration of renewable energy sources.

QAMAR NAVID received the B.S. degree in electronics engineering from The Islamia University Bahawalpur, Pakistan, and the M.S. degree in electrical engineering from the Technical University of Dortmund, Germany. He is currently pursuing the Ph.D. degree in control sciences and engineering with the Beijing Institute of Technology, Beijing, China. He served two years with Hagel Automation GmbH, Germany, as an Automation Engineer and four years with UAE University as a Senior Researcher. He has published four journal articles in sustainability and batteries and one IEEE conference. His research interests include power systems, microgrid, renewable energy, fault detection and diagnostics, and low power energy storage components.

KHURSHEED AURANGZEB (Senior Member, IEEE) received the B.S. degree in computer engineering from the COMSATS Institute of Information Technology Abbottabad, Pakistan, in 2006, the M.S. degree in electrical engineering (system on chip design) from Linkoping University, Sweden, in 2009, and the Ph.D. degree in electronics design from Mid Sweden University, Sweden, in June 2013. He is currently an Associate Professor with the Department of Computer Engineering, College of Computer and Information Sciences, King Saud University (KSU), Riyadh, Saudi Arabia. He has authored and coauthored more than 90 publications including, IEEE/ACM/Springer/Hindawi/MDPI journals, and flagship conference papers. He has obtained more than 15 years of excellent experience as an Instructor and a Researcher in data analytics, machine/deep learning, signal processing, electronics circuits/systems, and embedded systems. He has been involved in many research projects as a Principal Investigator and a Co-Principal Investigator. His research interests include the diverse fields of embedded systems, computer architecture, signal processing, wireless sensor networks, communication, and camera-based sensor networks with an emphasis on big data and machine/deep learning with applications in smart grids, precision agriculture, and healthcare.

MUHAMMAD SHAHID ANWAR is currently an Assistant Professor with Gachon University, his research focus is to evaluate VR remote health and telemedicine systems. The main research activities are investigating the influencing factor and different aspects that affect the QoE of AR/VR/MR systems. He is passionate about user research and user involvement in user-centric innovation processes and the activities are linked to human-technology experiences i.e., quality of experience, user engagement, and immersive experiences (AR/VR/XR) and human-technology behavior, related methodological challenges. He had also worked on QoE measurement and QoE-based optimization to foster user delight, reduce user annoyance, and to enable pleasurable experiences. The system, human, and context factors influencing QoE for a range of applications and in different domains (e.g., 360-degree virtual reality videos and immersive media, interactive services, and assistive technology in healthcare) were considered during the research. Different QoE influencing factors for 360-degree videos and aspects, such as perceptual quality, immersion and presence, cybersickness, reality judgment, user engagement, and attention captivation were evaluated during several subjective experiments. He has proposed and modeled several machine learning algorithms for the prediction of QoE of 360-degree VR video.